Supplementary Materials for

The Critical Role of the 2'-OH group in Phase Separation and Percolation Transitions of RNA

Authors: Gable M. Wadsworth[1]†, Dilimulati Aierken[2,3]†, George M. Thurston[4], Jerelle A. Joseph[2,3]*, Priya R. Banerjee[1]*

Affiliations:

[1] Department of Physics, The State University of New York at Buffalo; Buffalo, NY 14260, USA.

[2] Department of Chemical and Biological Engineering, Princeton University, Princeton, NJ 08544, USA.

[3] Omenn–Darling Biological Engineering Institute, Princeton University, Princeton, NJ 08544, USA.

[4] School of Physics and Astronomy, Rochester Institute of Technology, Rochester, New York 14623, USA.

† These authors contributed equally

* Correspondence should be addressed to: P.R.B (prbanerj@buffalo.edu); J.A.J (jerellejoseph@princeton.edu)

The PDF file includes:

Other Supplementary Materials for this manuscript include the following:

Materials and Methods

Simulations

Atomistic simulations of CAG repeats:

We perform atomistic molecular dynamics (MD) simulations of CAG repeats using CHARMM36m [1,2] force field with TIP3P [3] water model. CHARMM36m includes parameterizations of post-transcriptionally modified ribonucleotides [4], which aligns well with the goal of this study. For all simulations, we use GROMACS [5,6] package (Version 2023.3) on GPUs via Princeton Research Computing Clusters. Initial states of the systems are generated using CHARM-GUI [7,8]. To prepare the systems, $r(CAG)_6$, $r(CmAG)_6$, and $d(CAG)_6$ are solvated in an 80Å×80Å×80Å cubic box. Mg^{2+} or Ca^{2+} ions, along with Cl^- ions, are added to achieve the target divalent salt concentration of 150mM (~55,000 atoms in total). We then perform energy minimization via the steepest descent method, followed by a short equilibration (500–700 ps) in the *NVT*-ensemble using V-rescale algorithm for temperature coupling (T = 293 K or 368 K) to obtain different initial structures. Finally, the 600-ns production run is performed in the *NPT*-ensemble, employing V-rescale algorithm for temperature coupling and C-rescale algorithm for pressure coupling at T = 293 K/368 K and p= 1 bar. The data from the last 500ns is used for data analysis. In all simulations, periodic boundary conditions are imposed, the PME [9] algorithm is used for long-range electrostatic interactions, and LINCS [10] algorithm is employed for H-bond constraints. Each polymer is run for three independent simulations, yielding aggregate simulation times of ca. 1,500 ns. MDAnalysis package [11] is used for all trajectory analysis, and Pymol [12] and UCSF ChimeraX [13] are used for visualizations and schematics.

Minimal model simulations of AB systems:

To study the impact of chain stiffness on condensate properties, we conduct minimal model MD simulations. We design an AB-type model, where only A and B form associative interactions mimicking complementary base pairing. The bonded interactions are modeled by a harmonic potential, the excluded volume potential of same-type interactions (A–A and B–B) are modeled via the Weeks–Chandler–Andersen (WCA) potential, and the attractive interaction is modeled by Lennard-Jones (LJ) potential. We simulate identical chains with the primary sequence of $(AB)_{25}$ and systems are composed of 125 chains. The bending stiffness is modeled by the typical cos potential, and we only vary the relative stiffness in our simulations to evaluate the effect on condensate properties. In the MD simulations, we use Lennard-Jones units and integration of equations of motion is carried out in the LAMMPS [14] package (23 June 2022 Version). Each system is simulated in the *NVT*-ensemble, employing a Langevin thermostat. The masses of the monomers are set to m=1, the monomer size and equilibrium bond length are set to σ=1, and the LJ potential minimum is set to ε=1. The excluded volume strength is also set to ε, and the bonded interaction is set to 10ε, and the bending stiffness κ is varied from 2ε to 12ε. Finally, the simulation temperature is set to kT/ε = 0.8, with damping constant 0.5τ. The simulations are performed for at least for 60,000,000 steps with the step size of 0.005τ to ensure proper equilibration. 1000 snapshots from the last 10,000,000 steps, which are sampled every 10,000 steps, are taken for analysis. For the droplet shape and neighbor analysis Ovito [15] is used. For the local order analysis, Q-tensor analysis is performed using custom codes.

Nucleic acid sample preparation for temperature-controlled microscopy:

Nucleic acids are obtained from Integrated DNA Technologies using salt-free purification and are stored in RNase free water (Ambion) at stock concentrations at either 200 μM (RNA) or 1 mM (ssDNA). RNA homopolymers were obtained from Sigma-Aldrich [poly(rC), Sigma #P4903-25MG, Batch # 0000091053; poly(rU), Sigma #P9528-10MG, Lot #089M4052V] and reconstituted in RNase free water. 2'-O-methylated RNA were obtained from Gene Link and stored in RNase

free water. Nucleic acids were prepared in buffer as described in the text by diluting RNA into RNase free water mixed with a 4x buffer stock to a final working concentration described in the main text. DNA samples were observed to have some aggregates in the stock, which were removed by spinning at 10,000 rpm and retaining the supernatant. The concentration of DNA in the supernatant was recorded.

Nucleic acid samples for phase separation assays were prepared as described previously [16,17]. In brief, glass slides were cut to fit the temperature stage to be approximately 1"x 0.8" using a carbide glass scribe (Thorlabs). Slides were cleaned using ethanol and kimwipes and then two strips of double-sided tape (Scotch) are placed approximately 1 mm apart with 18 mm square #1.5 coverslip placed on top. These channels can contain approximately 5 µL of sample. A small drop of 518N oil is placed at either end of the channel to prevent evaporation after filling. Samples were imaged immediately after preparation.

For samples that were tested with variation of pH, buffers containing equimolar concentrations of HEPES, MES, and sodium acetate were prepared at evenly spaced intervals of one pH unit by titrating with HCl. This buffer has previously been reported to have a linear behavior in the range of pH 2-8 [18]. Samples were then subjected to measurements using temperature-controlled microscopy.

Temperature-dependent microscopy of RNA and DNA:

Samples were imaged via temperature-controlled microscopy as previously described [16,17]. In brief, an Instec temperature-controlled stage was used to sweep temperatures between 0°C to 90°C. Temperature was set manually using the ramp setting which heats at ~5°C/min. Near T_{phase} of a sample, the temperature was increased in 2°C increments every 5 minutes. The sample was cycled around T_{phase} at least once beyond the initial measurement to confirm (or a lack thereof) reversibility. Temperature values were extracted using a K-type thermocouple in combination with a USB digital to analog converter. This outputs temperatures with time stamps that are aligned with each frame time using image metadata through custom python code. A Zeiss primovert microscope was used with a 40x air objective and a Blackfly S camera (Teledyne FLIR) controlled via Micromanager to acquire images at 1 second intervals. T_{phase} values were extracted from three technical replicates.

Estimation of the percolation temperature (T_{prc}) via shape relaxation:

Videos of samples with percolation coupled to phase separation were identified and the temperatures of the start and end of shape relaxation were extracted manually through time-lapse image analysis. Here we define shape relaxation to be a change in particle size and/or morphology starting from an irregular cluster and ending in an energetically minimized circular shape. The width of these clusters was determined using Fiji to draw a line to reference the difference in size between two frames. All condensates of similar size relax at similar temperatures in a single image. A minimum of three trials were averaged to determine the start and end temperatures for shape relaxation and T_{prc} was assigned to be the average of these temperatures.

Small-angle X-ray scattering experiments and analysis:

Small-angle x-ray scattering experiments were conducted using the BioSAXS facilities at the Cornell High Energy Synchrotron Source (CHESS). These experiments entailed preparation of RNA and ssDNA in equivalent buffer conditions with varying concentrations of magnesium ions. Samples were prepared by spinning defrosted stocks of nucleic acids for 10 minutes before dilution in buffer containing 50 mM HEPES, pH 7.5 at room temperature, and either 1 mM, 5 mM, or 10 mM $MgCl_2$. Stocks were kept on dry ice and transported to CHESS. Samples were thawed

and inserted into a 96-well plate where robotic handling transferred the solution to the capillary where it was imaged. Scattering images of the empty capillary tube and water-filled capillary tube were collected for subtraction and applied in the relevant options in the RAW software. The sample was dithered during imaging and 100 images were captured without any meaningful changes in signal. These data were averaged and background from similarly acquired data for the buffer was subtracted after a DC-offset. Data was verified to be linear in the low-q regime, implying mono-dispersity. A Guinier fit was applied to estimate the radius of gyration using the freely available RAW software for SAXS analysis. For those data which had upturns at low q Guinier fitting was constrained to have $q_{min}*R_g \sim 0.65$ where the residuals for the fit were found to be randomly distributed.

Data analysis and preparation:

All experimental data was plotted using custom python scripts relying on the Numpy, Scipy, and Matplotlib libraries including the data processed using RAW. Figures in the main text were prepared using Adobe Illustrator and for chemical structures, ChemDraw, was used.

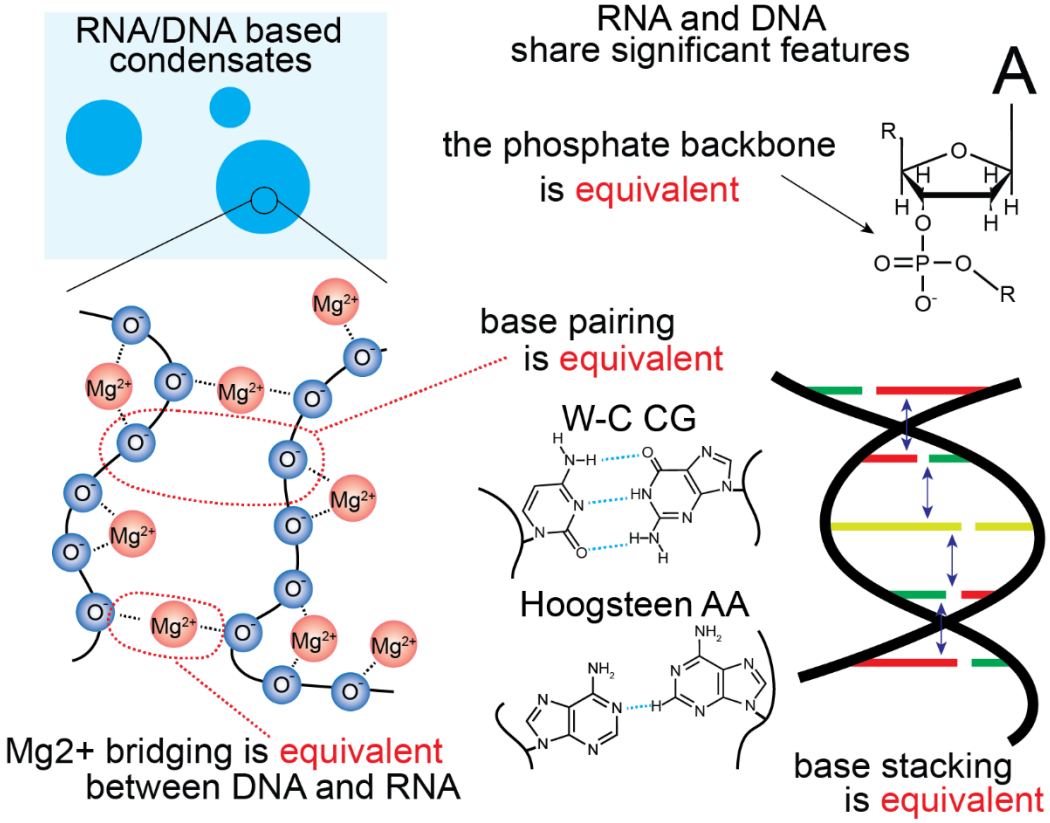

Fig. S1. Cartoon representations of the different modes of interactions of single stranded nucleic acids. While often described through their differences, many features of DNA and RNA are shared. The means of crosslinking are identical between ssDNA and RNA. The sole difference is the 2'-OH of ribose.

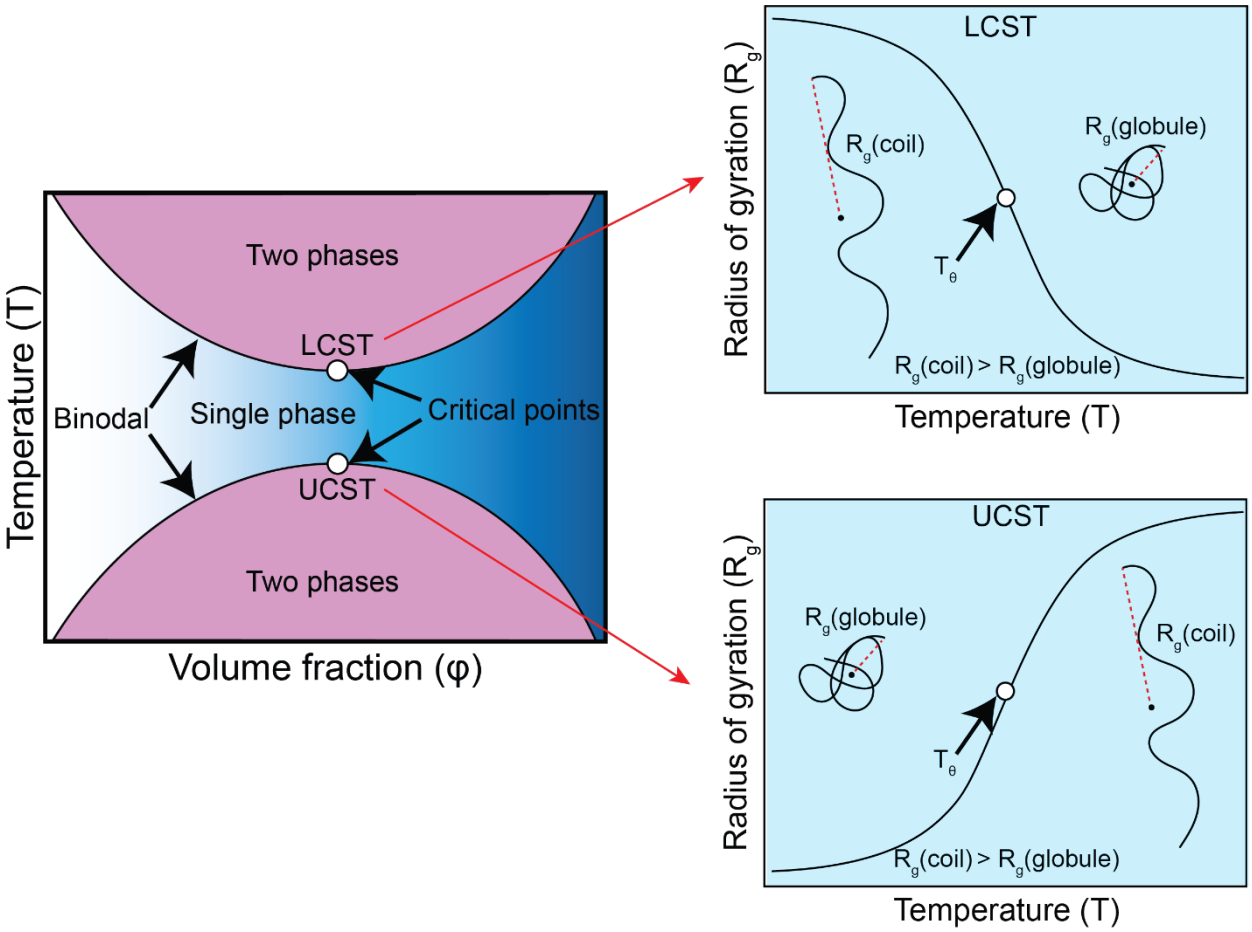

164

165

166 **Fig. S2. Lower and Upper Critical Solution Temperature (UCST/LCST)-type phase**
167 **separation accompanies a corresponding coil-to-globule transition of the single chain.** A
168 schematic showing that as the solution approaches the binodal and begins to undergo phase
169 separation, there is an associated collapse of single chains known as a coil-to-globule transition.
170 This transition occurs while cooling for polymers with UCSTs and during heating for polymers with
171 LCSTs.

172

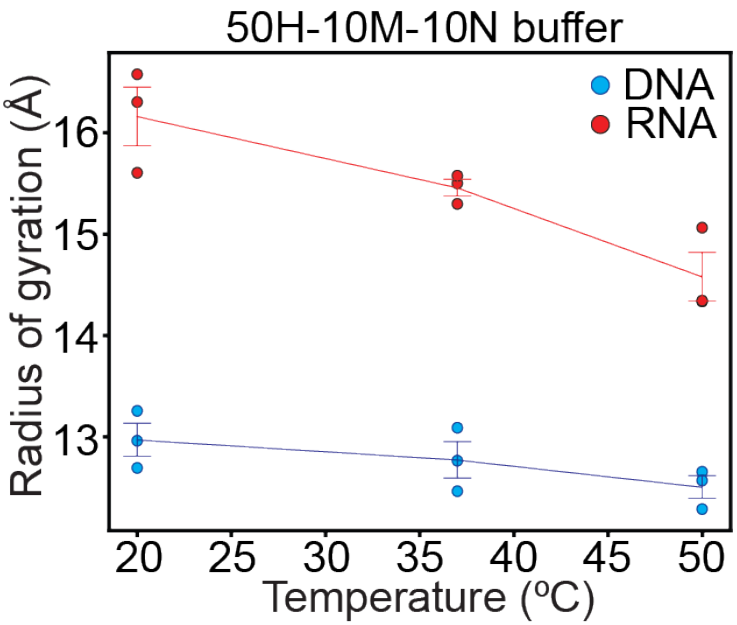

Fig. S3. Radius of gyration (R_g) estimation of short $(CAG)_6$ RNA and ssDNA using Small Angle X-ray Scattering (SAXS). Comparison of the temperature dependence of R_g estimated through Guinier fitting of SAXS data for 50 μM $(CAG)_6$ RNA (red) with ssDNA (blue) in a buffer containing 50 mM HEPES, pH 7.5 at RT, with 10 mM $MgCl_2$ and 10 mM NaCl. Buffer notation used: the number in front of "H" indicates the [HEPES] in mM, the number in front of "M" indicates the [$MgCl_2$] in mM, and the number in front of "N" indicates the [NaCl] in mM for each buffer. Error bars represent s.e.m. for n = 3 replicates.

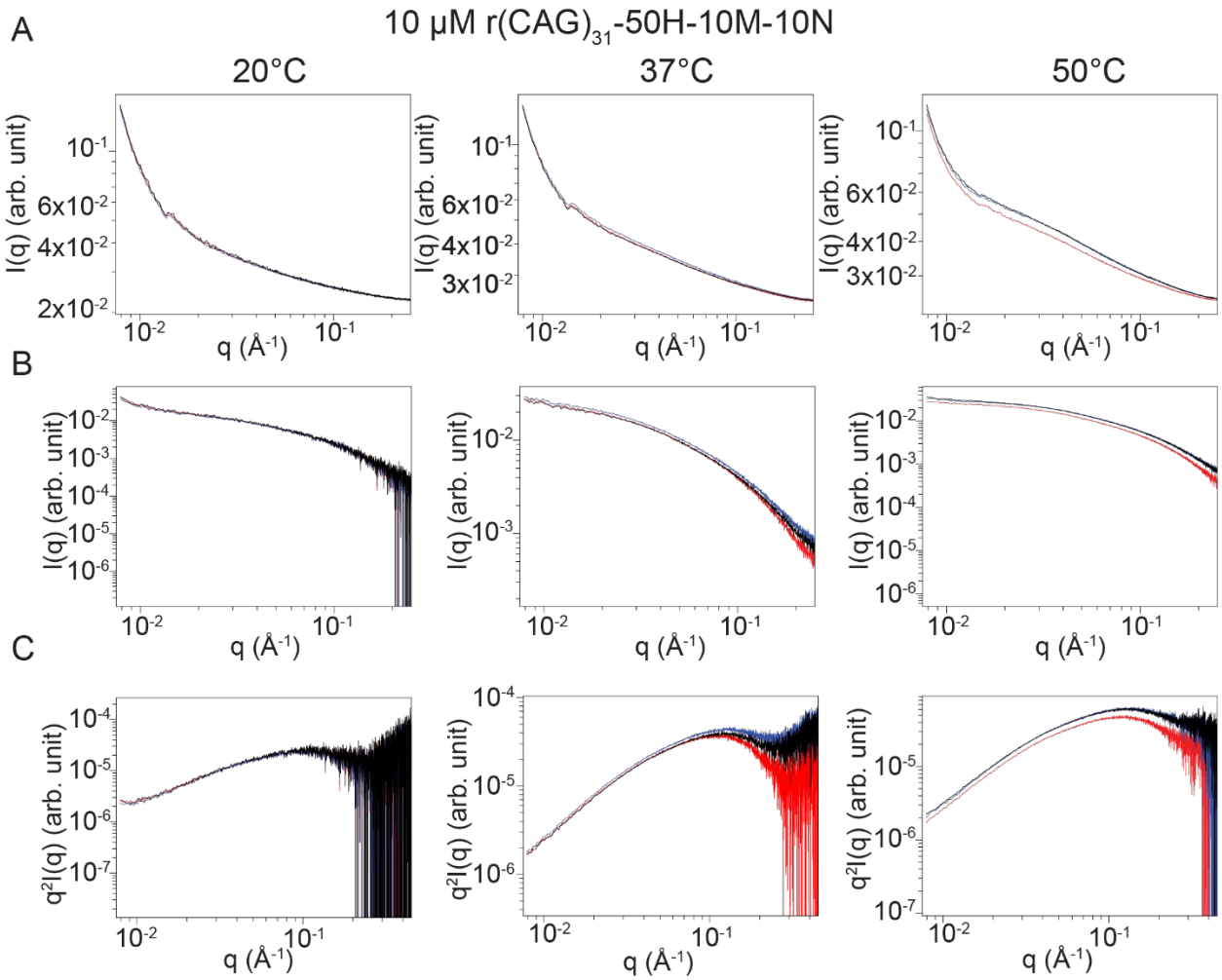

185

186 **Fig. S4. Small Angle X-ray Scattering (SAXS) data for $(CAG)_{31}$ RNA. A.** Temperature
187 dependence of SAXS data for 10 μM $(CAG)_{31}$ RNA with three trials (red, blue, black) in a buffer
188 containing 50 mM HEPES, pH 7.5 at RT, with 10 mM $MgCl_2$ and 10 mM NaCl. Data is averaged
189 over ~100 frames and normalized to an absolute scale using water. **B.** Subtracted SAXS data
190 from **A.** An acquisition of buffer solution including ions was averaged over ~100 frames and used
191 for subtraction. **C.** Kratky diagrams of the data from **B.** Buffer notation used: the number in front
192 of "H" indicates the [HEPES] in mM, the number in front of "M" indicates the [$MgCl_2$] in mM, and
193 the number in front of "N" indicates the [NaCl] in mM for each buffer.
194

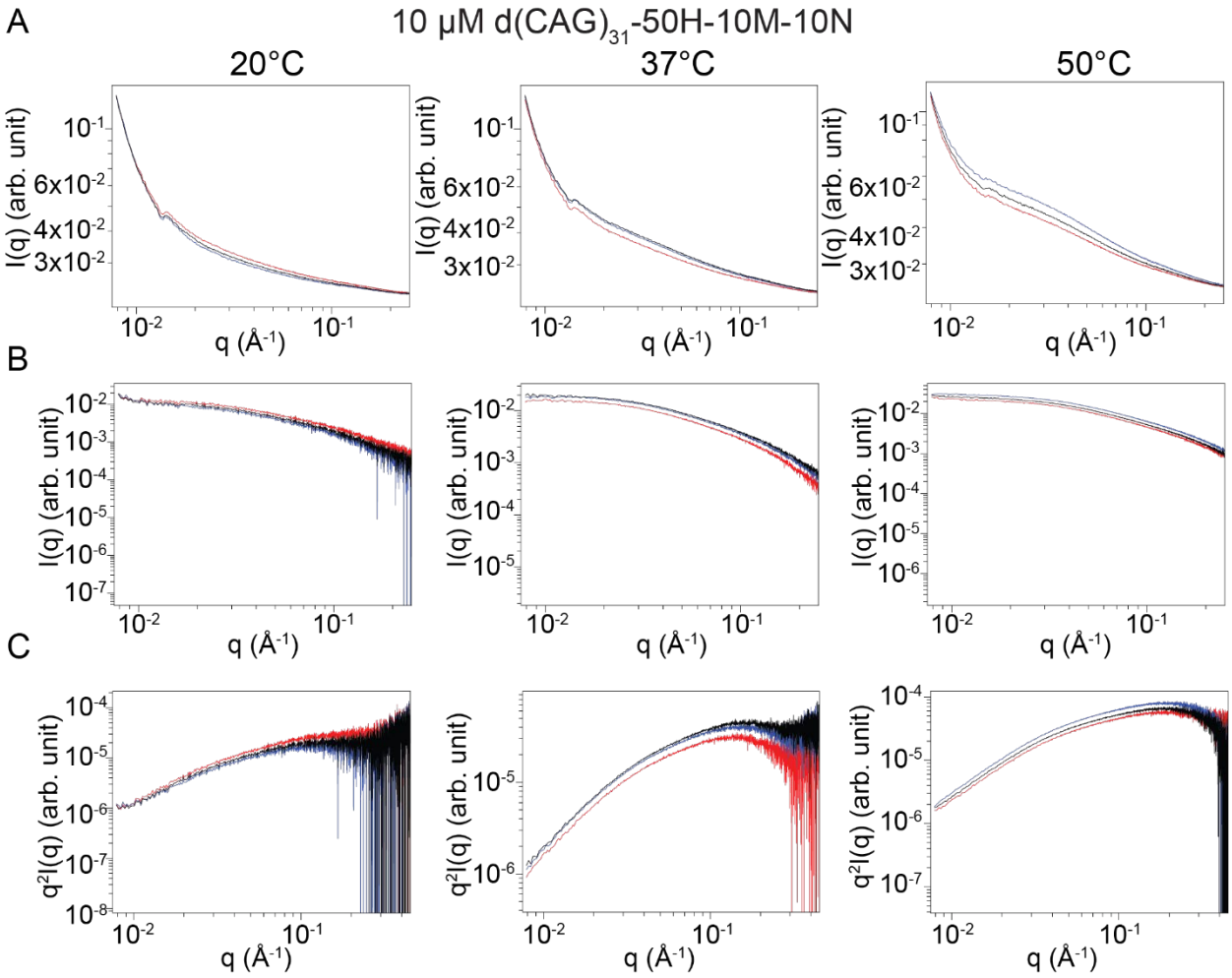

Fig. S5. Small Angle X-ray Scattering (SAXS) data for $(CAG)_{31}$ ssDNA. A. Temperature dependence of SAXS data for 10 μM $(CAG)_{31}$ DNA with three trials (red, blue, black) in a buffer containing 50 mM HEPES, pH 7.5 at RT, with 10 mM $MgCl_2$ and 10mM NaCl. Data is averaged over ~100 frames and normalized to an absolute scale using water. **B.** Subtracted SAXS data from **A.** An acquisition of buffer solution including ions was averaged over ~100 frames and used for subtraction. **C.** Kratky diagrams of the data from **B.** Buffer notation used: the number in front of "H" indicates the [HEPES] in mM, the number in front of "M" indicates the [$MgCl_2$] in mM, and the number in front of "N" indicates the [NaCl] in mM for each buffer.

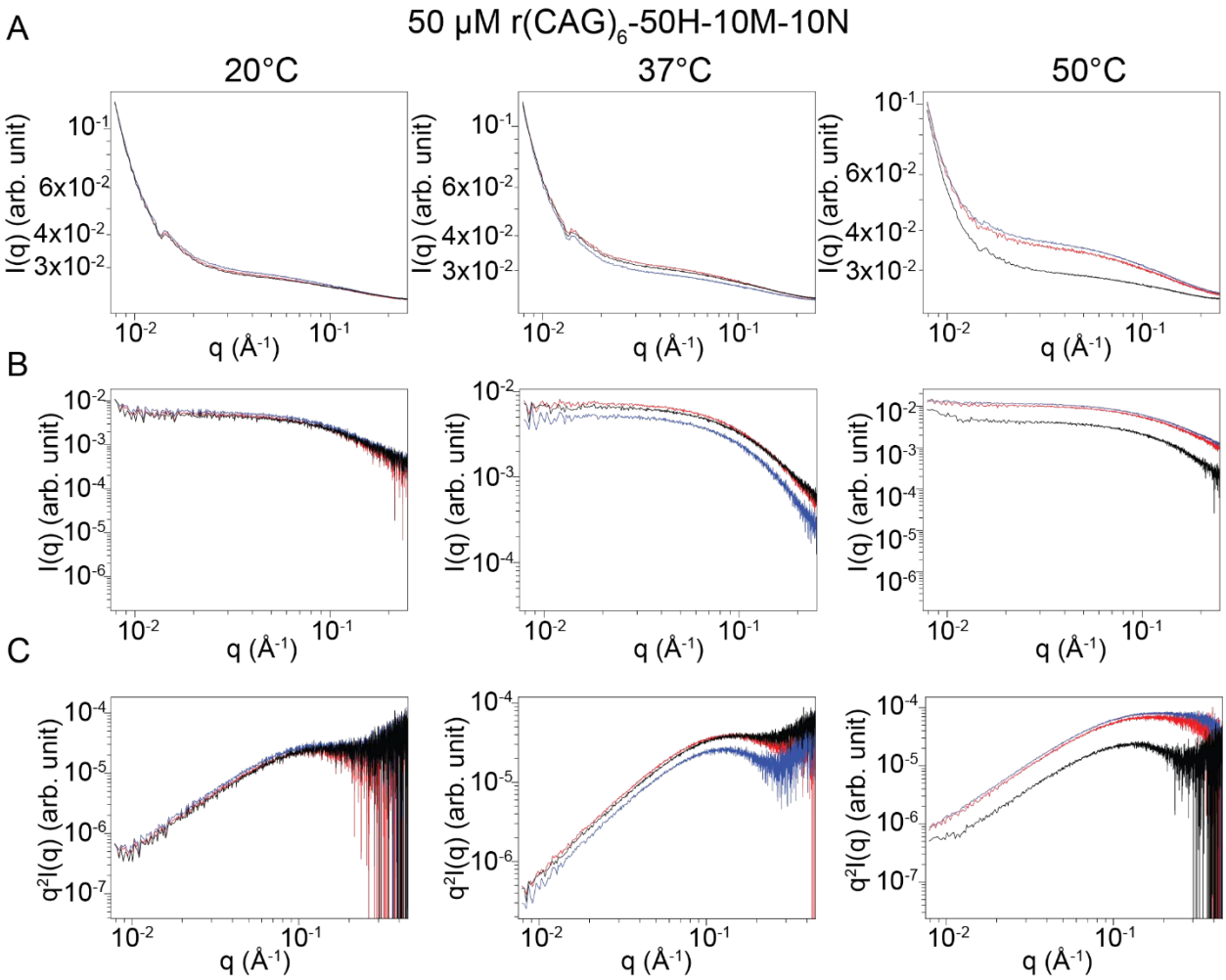

205

206 **Fig. S6. Small Angle X-ray Scattering (SAXS) data for $(CAG)_6$ RNA. A.** Temperature
207 dependence of SAXS data for 50μM $(CAG)_6$ RNA with three trials (red, blue, black) in a buffer
208 containing 50 mM HEPES, pH 7.5 at RT, with 10 mM $MgCl_2$ and 10 mM NaCl. Data is averaged
209 over ~100 frames and normalized to an absolute scale using water. **B.** Subtracted SAXS data
210 from **A.** An acquisition of buffer solution including ions was averaged over ~100 frames and used
211 for subtraction. **C.** Kratky diagrams of the data from **B.** Buffer notation used: the number in front
212 of "H" indicates the [HEPES] in mM, the number in front of "M" indicates the [$MgCl_2$] in mM, and
213 the number in front of "N" indicates the [NaCl] in mM for each buffer.

214

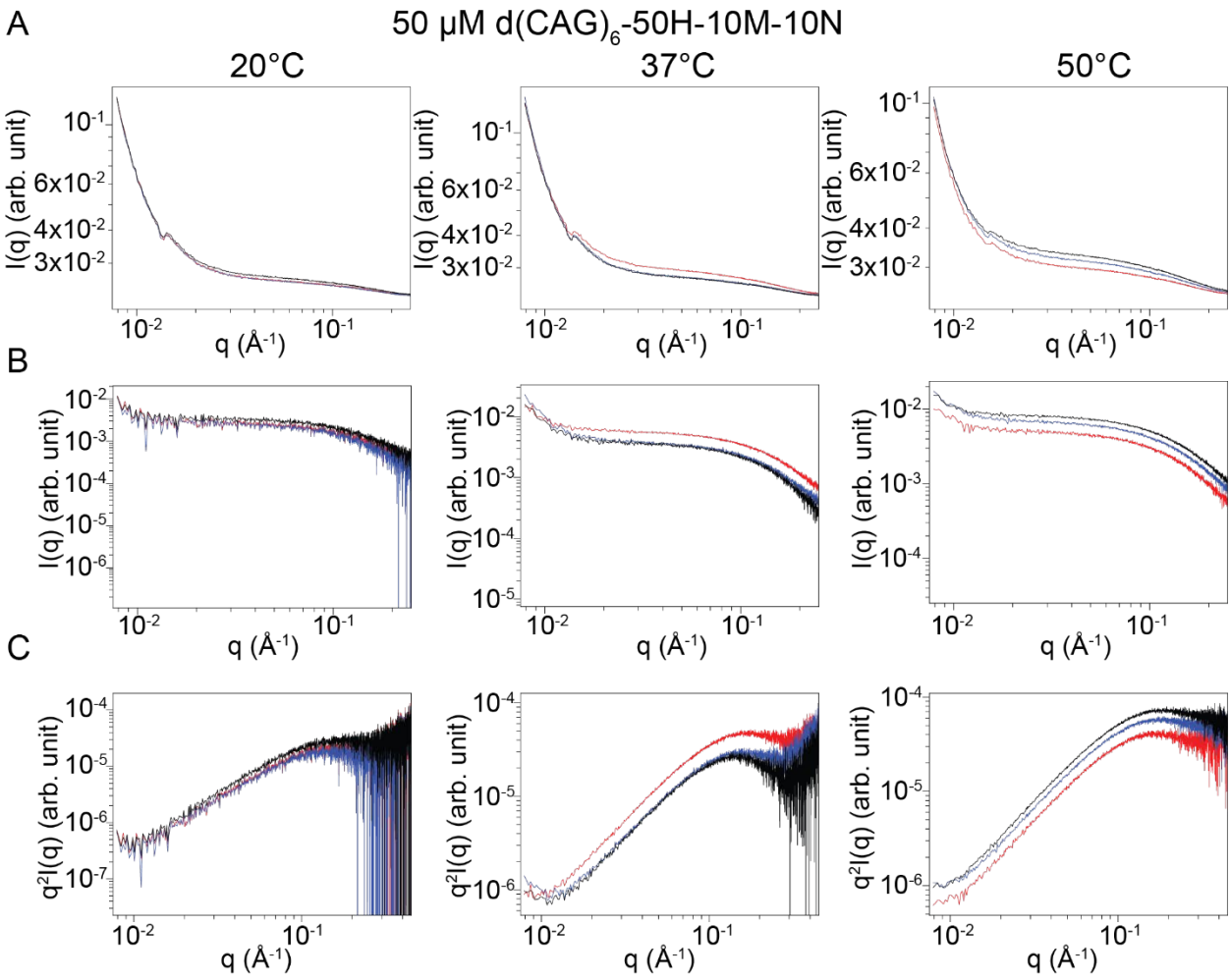

215

216

217 **Fig. S7. Small Angle X-ray Scattering (SAXS) data for $(CAG)_6$ DNA. A.** Temperature
218 dependence of SAXS data for 50 μM $(CAG)_6$ DNA with three trials (red, blue, black) in a buffer
219 containing 50 mM HEPES, pH 7.5 at RT, with 10 mM $MgCl_2$ and 10 mM NaCl. Data is averaged
220 over ~100 frames and normalized to an absolute scale using water. **B.** Subtracted SAXS data
221 from **A.** An acquisition of buffer solution including ions was averaged over ~100 frames and used
222 for subtraction. C. Kratky diagrams of the data from **B.** Buffer notation used: the number in front
223 of "H" indicates the [HEPES] in mM, the number in front of "M" indicates the [$MgCl_2$] in mM, and
224 the number in front of "N" indicates the [NaCl] in mM for each buffer.

225

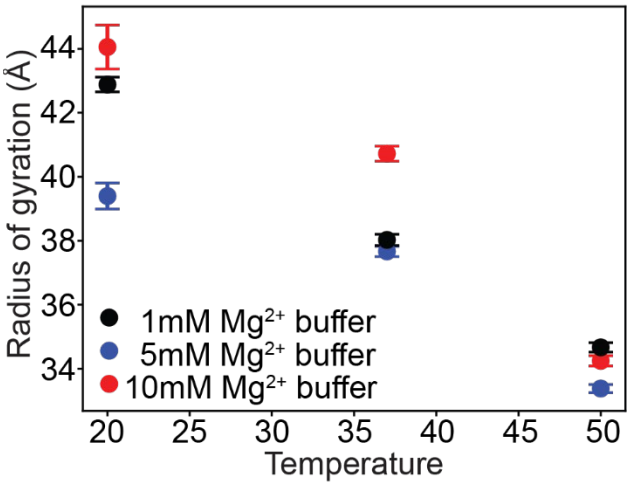

226

227 **Fig. S8. Magnesium ion dependent coil-to-globule transition of** $(CAG)_{31}$ **RNA.** Comparison
228 of the R_g of 10 μM $r(CAG)_{31}$ in a buffer containing 50 mM HEPES, pH 7.5 at RT, with $[MgCl_2]$ = 1
229 mM (black), 5 mM (blue), or 10 mM (red). Error bars represent s.e.m. for n = 3 replicates.

230
231

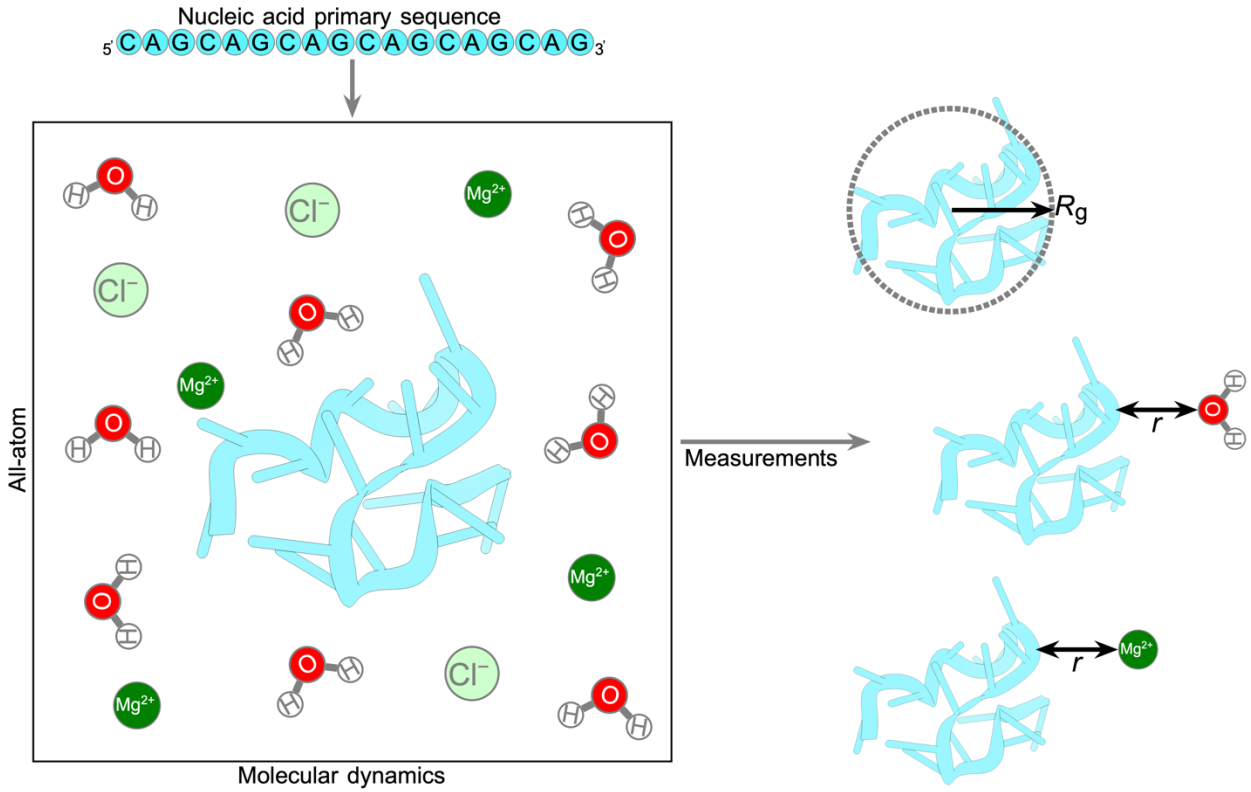

Fig. S9. Schematics of atomistic simulations. A schematic depicting the configuration of molecules in all-atom simulations is shown. The corresponding parameters radius of gyration, R_g, and the distance between phosphate oxygen (Op) in the backbone and the water or ions, r, are also depicted.

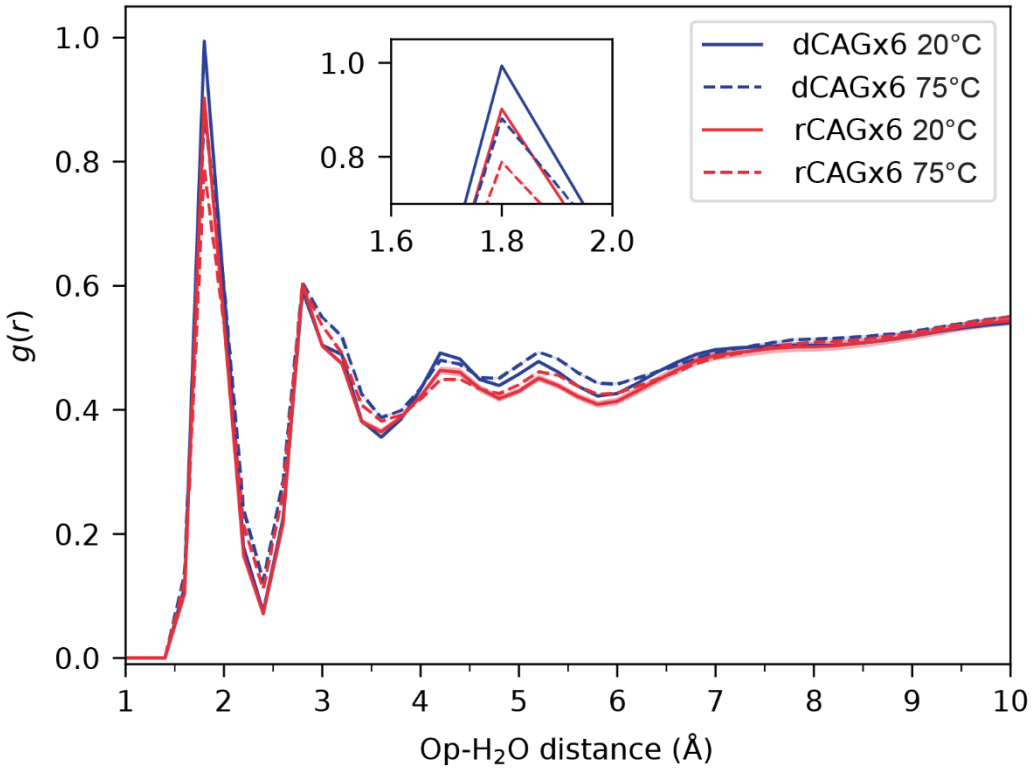

Fig. S10. Radial distribution of the distance between Op and H_2O in simulations with 150 mM $MgCl_2$. The normalized distribution of radial distances between phosphate oxygen (Op) and water molecules in simulations at two temperatures, 20°C (solid) and 75°C (dashed), for r$(CAG)_6$ (red) and d$(CAG)_6$ (blue). The errors are shown as error bands corresponding to three independent simulations.

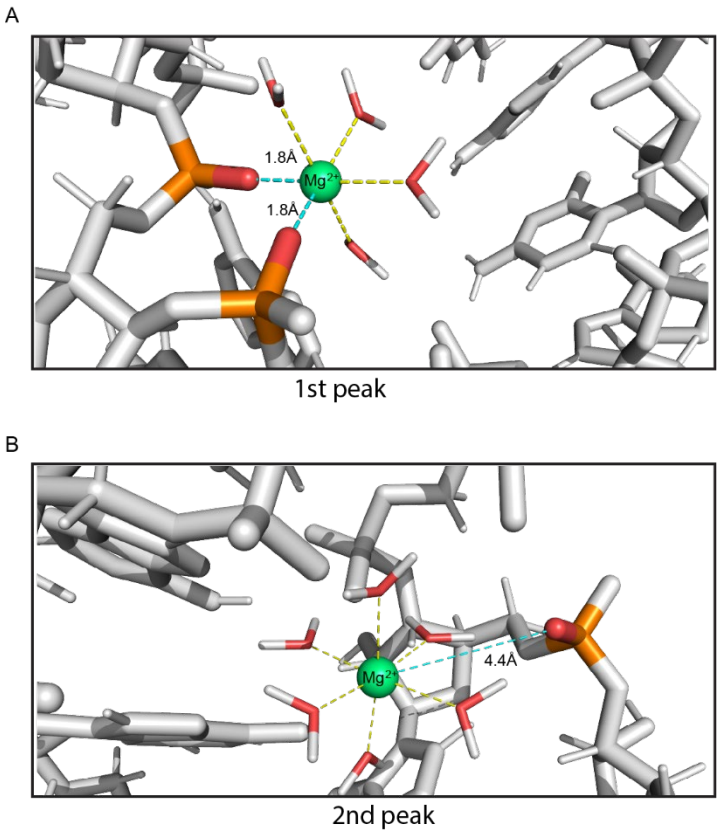

244

245

246 **Fig. S11. Relative proximity of Mg^{2+} ions from phosphate oxygen (Op)**. The distance between
247 the Mg^{2+} ions and the waters (yellow dashes) and Op (blue dashes) is shown for Mg^{2+} ions within
248 the first solvation shell **(A)** and the second solvation shell **(B)**.

249

250

251

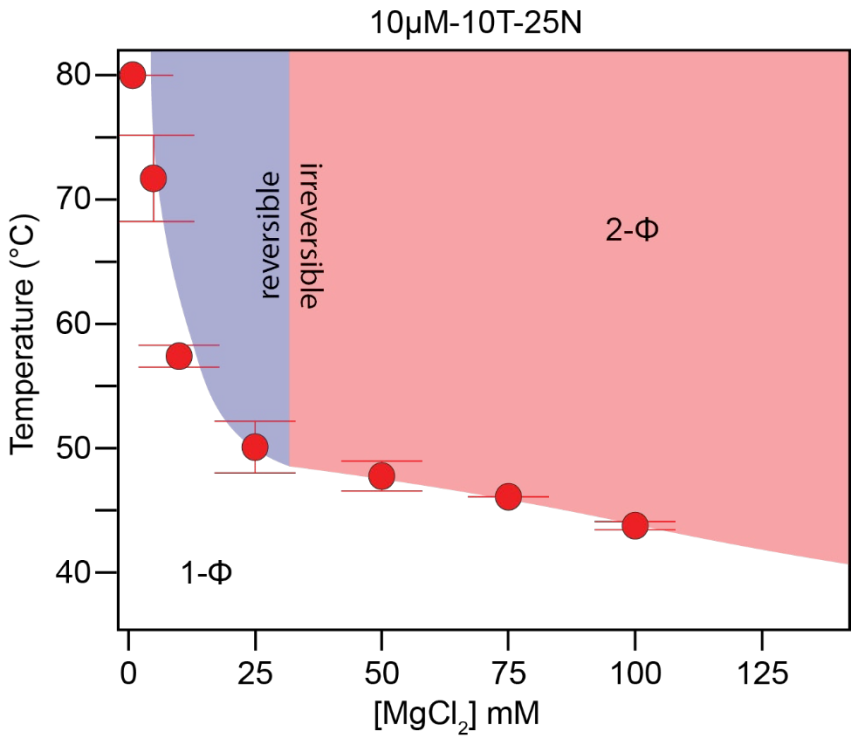

252

253 **Fig. S12. Mg^{2+} ion dependence of percolation for $r(CAG)_{31}$.** Data replotted from the SI of
254 Wadsworth, et al 2023 [17]. Shown here is a zoomed-in view of RNA state diagram from Figure 2C
255 to highlight the window of reversibility. The shaded region indicates the 2-Φ regime for $r(CAG)_{31}$
256 while the color indicates the reversibility (blue) or irreversibility (red). Buffer notation used: the
257 number in front of "T" indicates the [Tris-HCl] in mM, the number in front of "M" indicates the
258 [$MgCl_2$] in mM, and the number in front of "N" indicates the [NaCl] in mM in the buffer. Error bars
259 represent s.e.m. for n = 3 replicates.

260
261

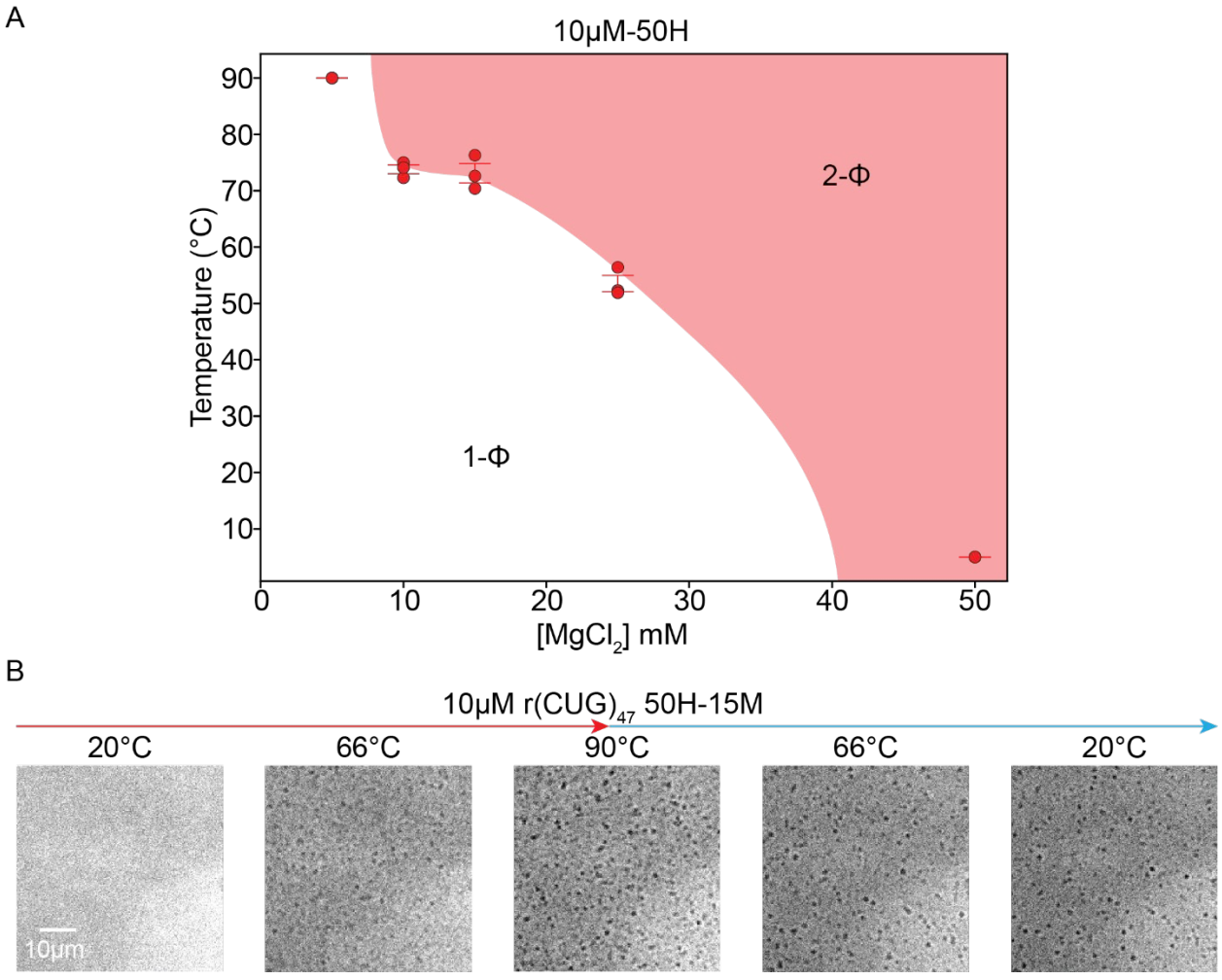

Fig. S13. $(CUG)_{47}$ RNA undergoes irreversible LCST-type phase transition. A. A state diagram showing the [$MgCl_2$] dependence of $r(CUG)_{47}$ phase behavior in a buffer containing 10 μM $r(CUG)_{47}$ and 50 mM HEPES, pH 7.5 at RT. The color and shading indicate irreversibility (red) of the 2-Φ regime (shaded). Error bars represent s.e.m. for n = 3 replicates. **B.** Representative images of thermoresponsive phase separation of 10 μM $r(CUG)_{47}$ in a buffer containing 50 mM HEPES, pH 7.5 at RT, and 15 mM $MgCl_2$. The LCPT of the sample is 66.3 ± 1.0°C. Buffer notation used: the number in front of "H" indicates the [HEPES] in mM and the number in front of "M" indicates the [$MgCl_2$] in mM in the buffer.

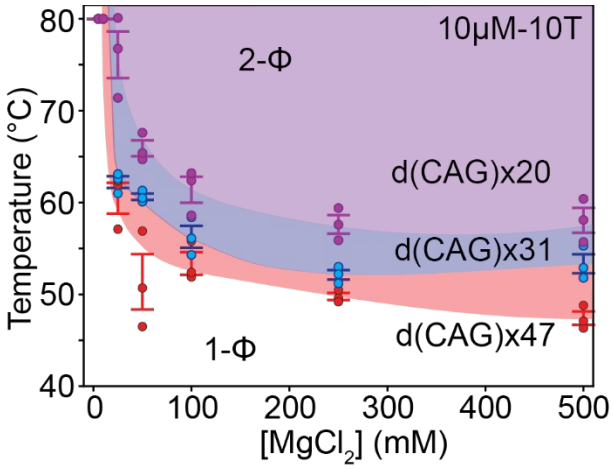

Fig. S14. Length dependence of phase separation for d(CAG)$_n$. A state diagram comparing the [$MgCl_2$] dependence of LCPTs for d(CAG)$_n$, where n = 20, 31, or 47. The shaded region indicates the 2-Φ regime for d(CAG)$_{47}$ (red), d(CAG)$_{31}$ (blue), and d(CAG)$_{20}$ (purple). Buffer notation used: the number in front of "T" indicates the [Tris-HCl] in mM in the buffer. Error bars represent s.e.m. for n = 3 replicates.

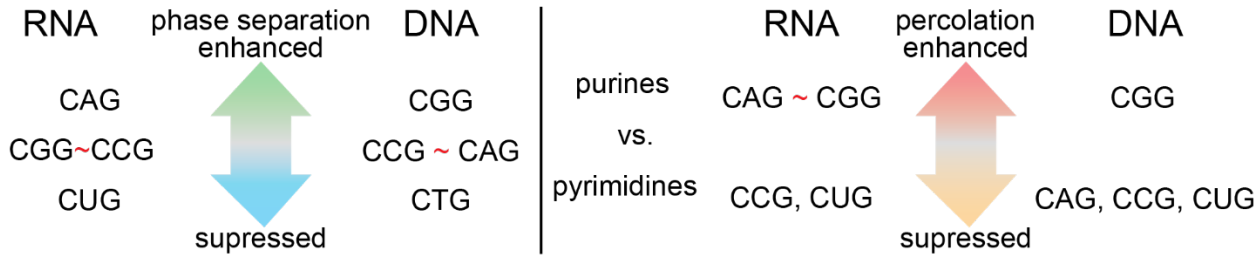

Fig. S15. Summary of the differences between RNA and DNA phase separation and percolation for $(CXG)_{31}$ repeats. The sequence dependence of phase separation and percolation are not equivalent. For RNA, CAG and CGG repeats display the strongest propensity to phase separate and percolate whereas CGG repeat DNA shows the strongest driving force for both phase separation and percolation.

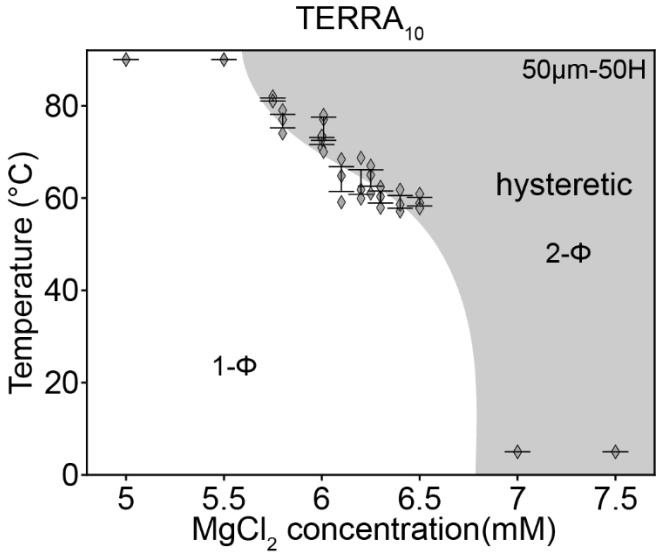

Fig. S16. $(TERRA)_{10}$ phase separation depends on the $MgCl_2$ concentration. A state diagram showing the [$MgCl_2$] dependence of $TERRA_{10}$ phase behavior in a buffer containing 50 µM $(TERRA)_{10}$ and 50 mM HEPES, pH 7.5 at RT. The color and shading indicate irreversibility (red) of the 2-Φ regime (shaded). Data is replotted from Mahendran et al. 2024 [16]. Buffer notation used: the number in front of "H" indicates the [HEPES] in mM in the buffer. Error bars represent s.e.m. for n = 3 replicates.

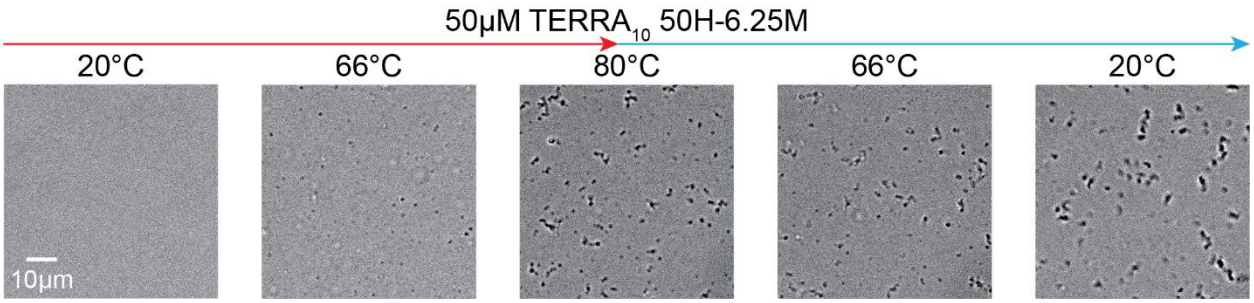

Fig. S17. Percolation of $(TERRA)_{10}$. Representative brightfield microscopy images of irreversible thermoresponsive phase separation of 50 μM $(TERRA)_{10}$ in a buffer containing 50 mM HEPES, pH 7.5 at RT, and 6 mM $MgCl_2$. The LCPT is 66.1 ± 1.8°C. Buffer notation used: the number in front of "H" indicates the [HEPES] in mM and the number in front of "M" indicates the [$MgCl_2$] in mM in the buffer.

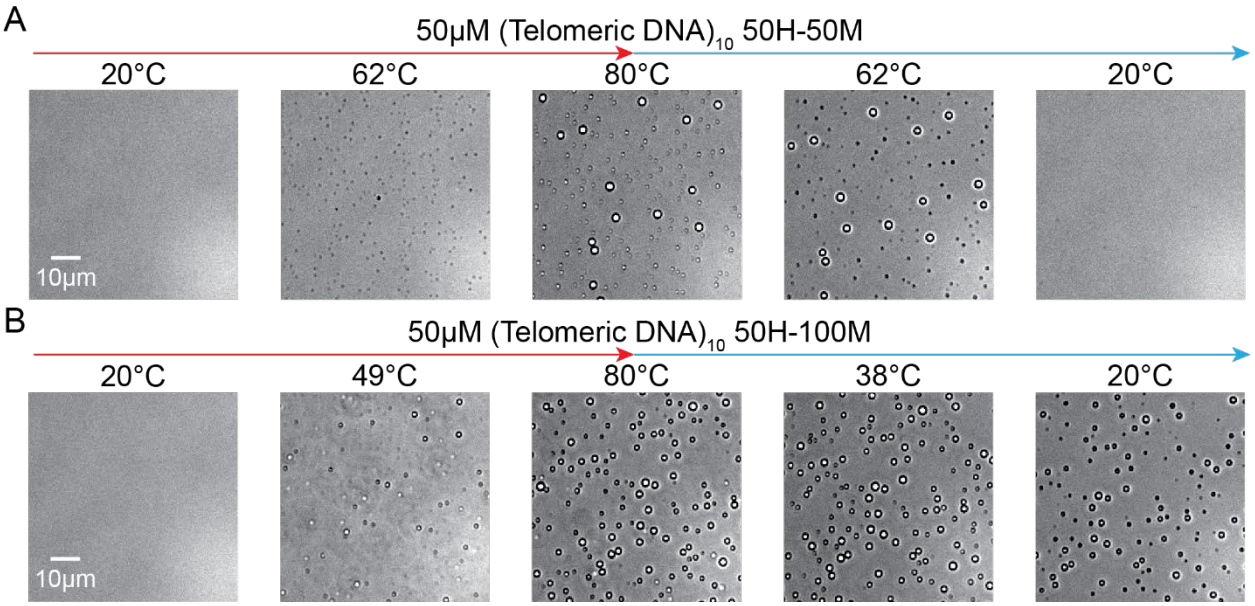

Fig. S18. Mg^{+2} ion concentration dependent reversible and irreversible phase separation of $(htelo)_{10}$. (A) Representative brightfield microscopy images of thermoresponsive phase separation of 50 μM $(htelo)_{10}$ in a buffer containing 50 mM HEPES, pH 7.5 at RT, and 50 mM $MgCl_2$. The LCPT is 60.4 ± 0.48°C. **(B)** Representative brightfield microscopy images of thermoresponsive phase separation of 50 μM $(htelo)_{10}$ in a buffer containing 50 mM HEPES, pH 7.5 at RT, and 100 mM $MgCl_2$. The LCPT is 49.2 ± 0.78°C. Buffer notation used: the number in front of "H" indicates the [HEPES] in mM and the number in front of "M" indicates the [$MgCl_2$] in mM in the buffer.

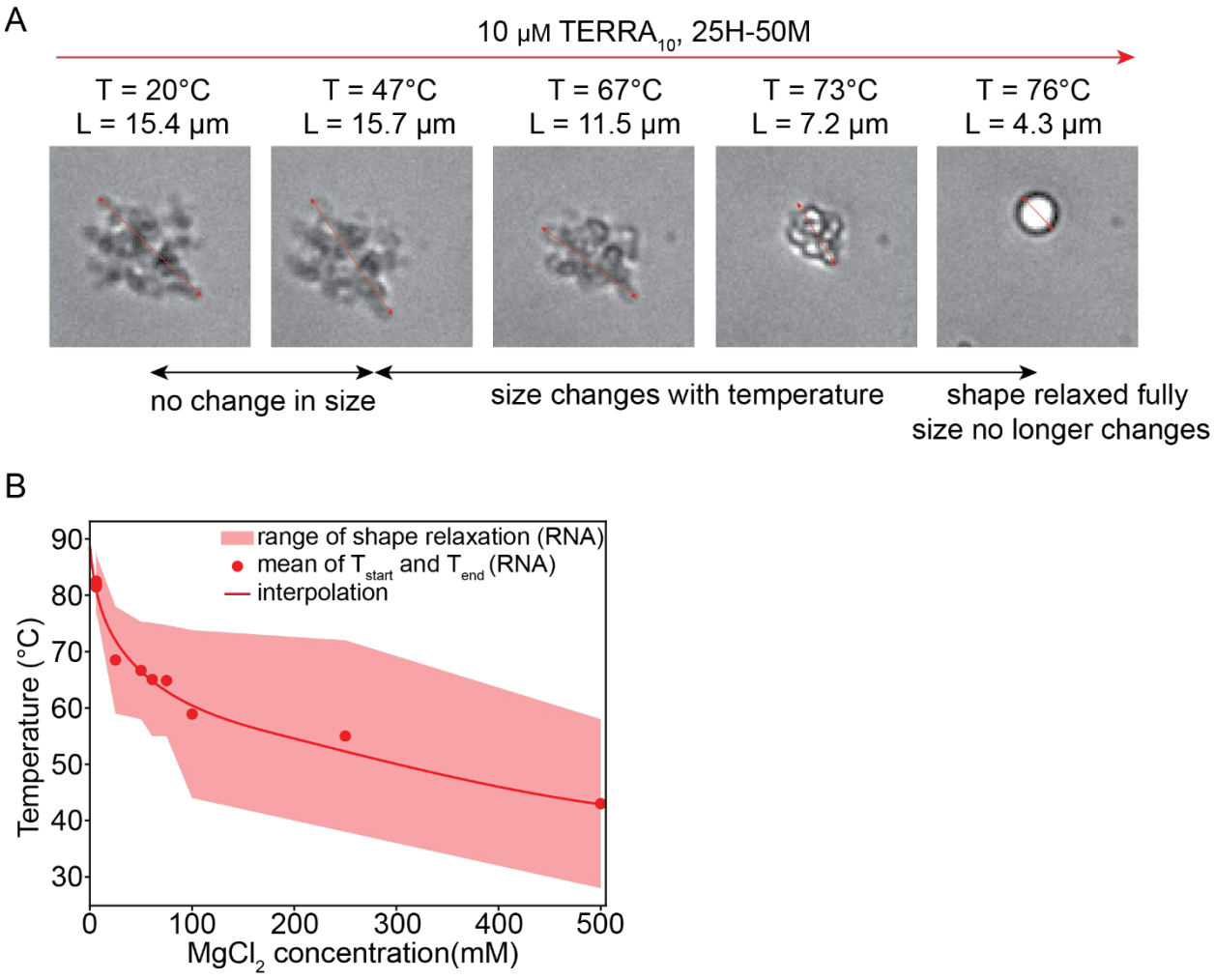

Fig. S19. Shape relaxation of percolated $(TERRA)_{10}$ condensates. A. Representative images of shape relaxation of $(TERRA)_{10}$ condensates during a thermal ramp. $(TERRA)_{10}$ condensates were formed utilizing 10 μM $TERRA_{10}$ in a buffer containing 25 mM HEPES, pH 7.5 at RT, and 50 mM $MgCl_2$. **(B)** A plot showing the upper and lower bounds of shape relaxation (boundaries of red shading) with the mean (red data) representing the percolation temperature (T_{prc}). Buffer notation used: the number in front of "H" indicates the [HEPES] in mM and the number in front of "M" indicates the [$MgCl_2$] in mM in the buffer.

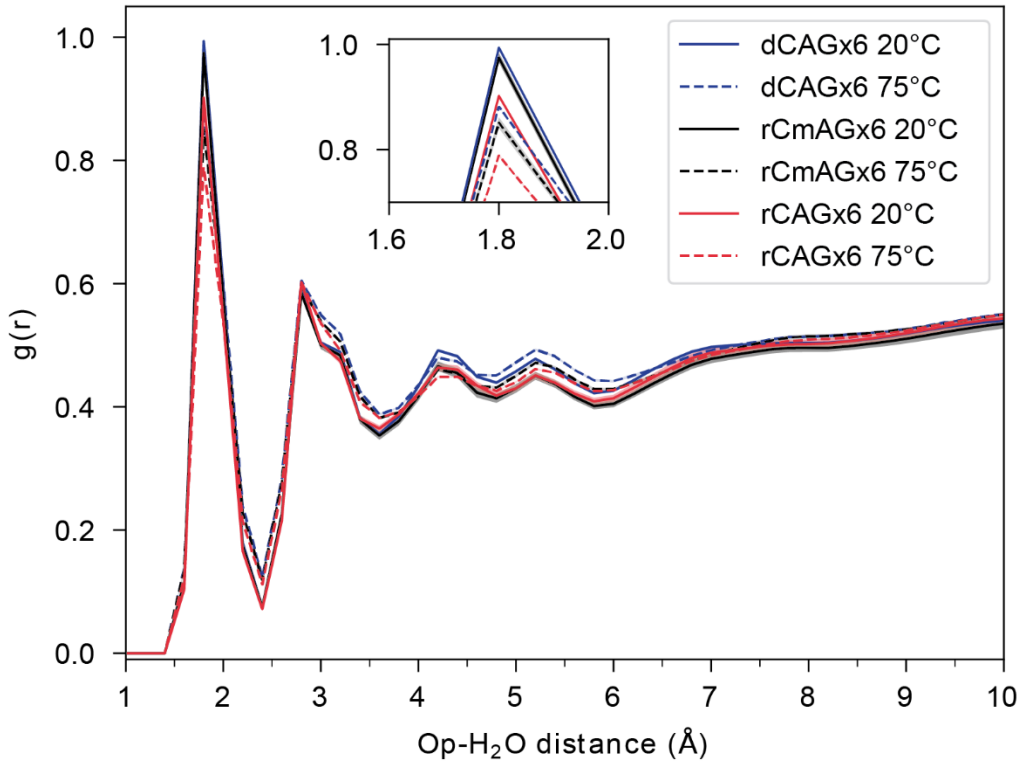

Fig. S20. Radial distribution of the distance between phosphate oxygen (Op) and H_2O for $r(CmAG)_6$ in simulations with 150 mM $MgCl_2$. The normalized radial distribution [$g(r)$] of distances between phosphate (Op) and water molecules in simulations at two temperatures, 20°C (solid) and 75°C (dashed), for $r(CAG)_6$ (red**),** $r(CmAG)_6$ (black), and $d(CAG)_6$ (blue). The errors are shown as error bands corresponding to three independent simulations.

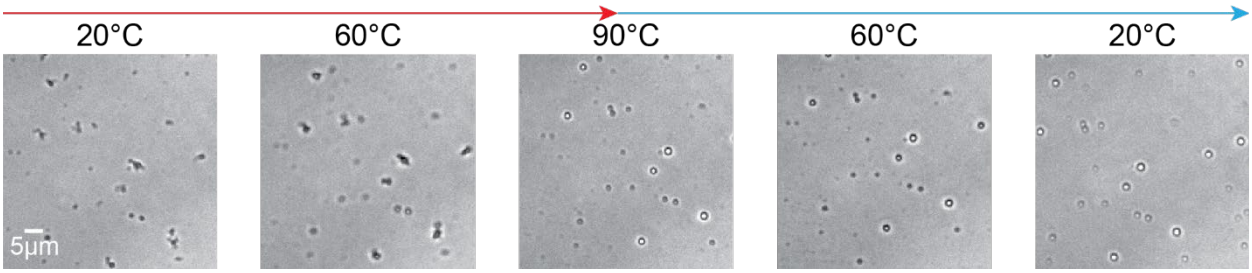

Fig. S21. Percolation of r(CmAG)$_{20}$ condensates in the presence of high concentrations of calcium ions. Shown is 10μM r(CmAG)$_{20}$ in a buffer containing 50 mM HEPES, pH 7.5 at RT, with 250 mM $CaCl_2$. The small clusters undergo shape relaxation as the temperature increases.

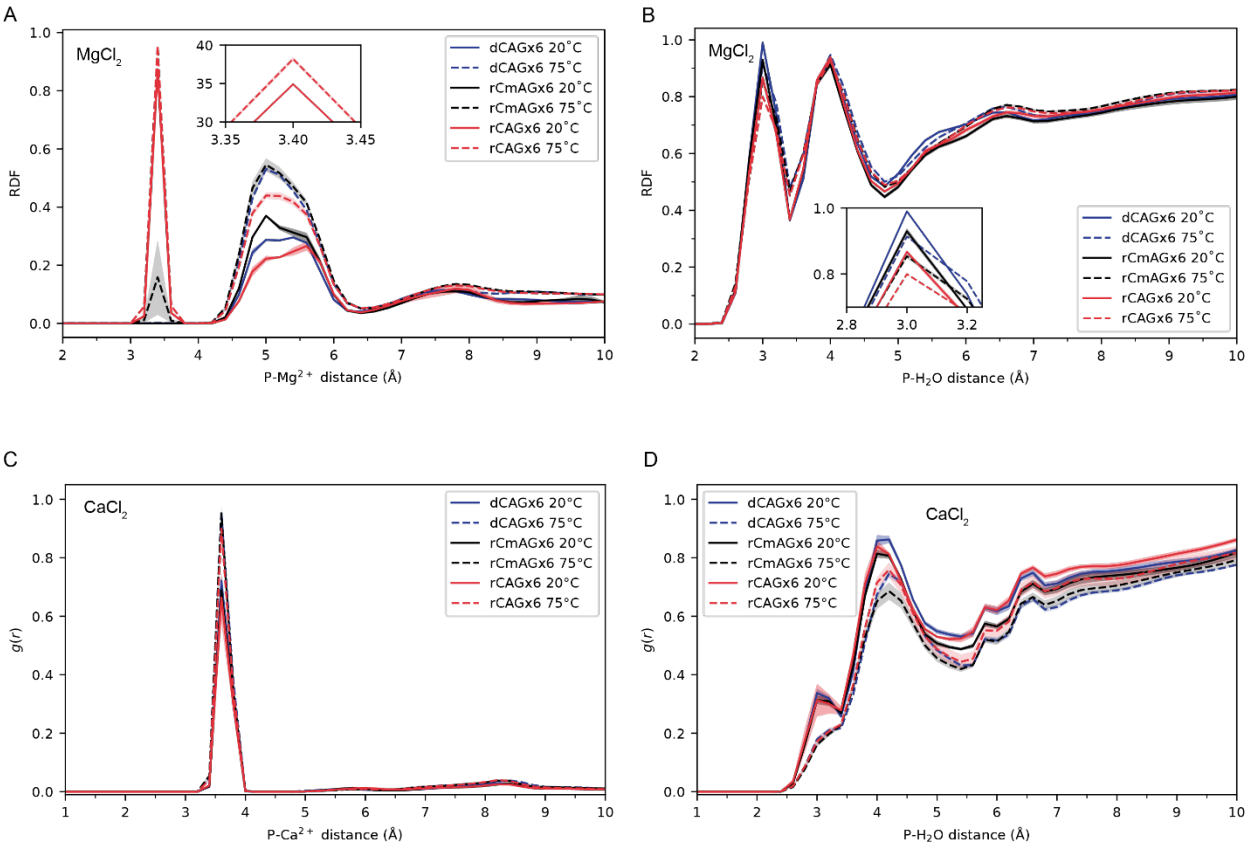

Fig. S22. Radial distribution of different ion types (Mg^{2+}/Ca^{2+}) relative to the backbone of nucleic acids (NAs), from atomistic simulations. The ion distribution (A, C) around the phosphate backbone and the water distribution (B, D) around the phosphate backbone. Whereas water molecules are more ordered around the backbone in the presence of Mg^{2+}, waters are more excluded from the backbone when Ca^{2+} is present. The errors are shown as error bands corresponding to three independent simulations.

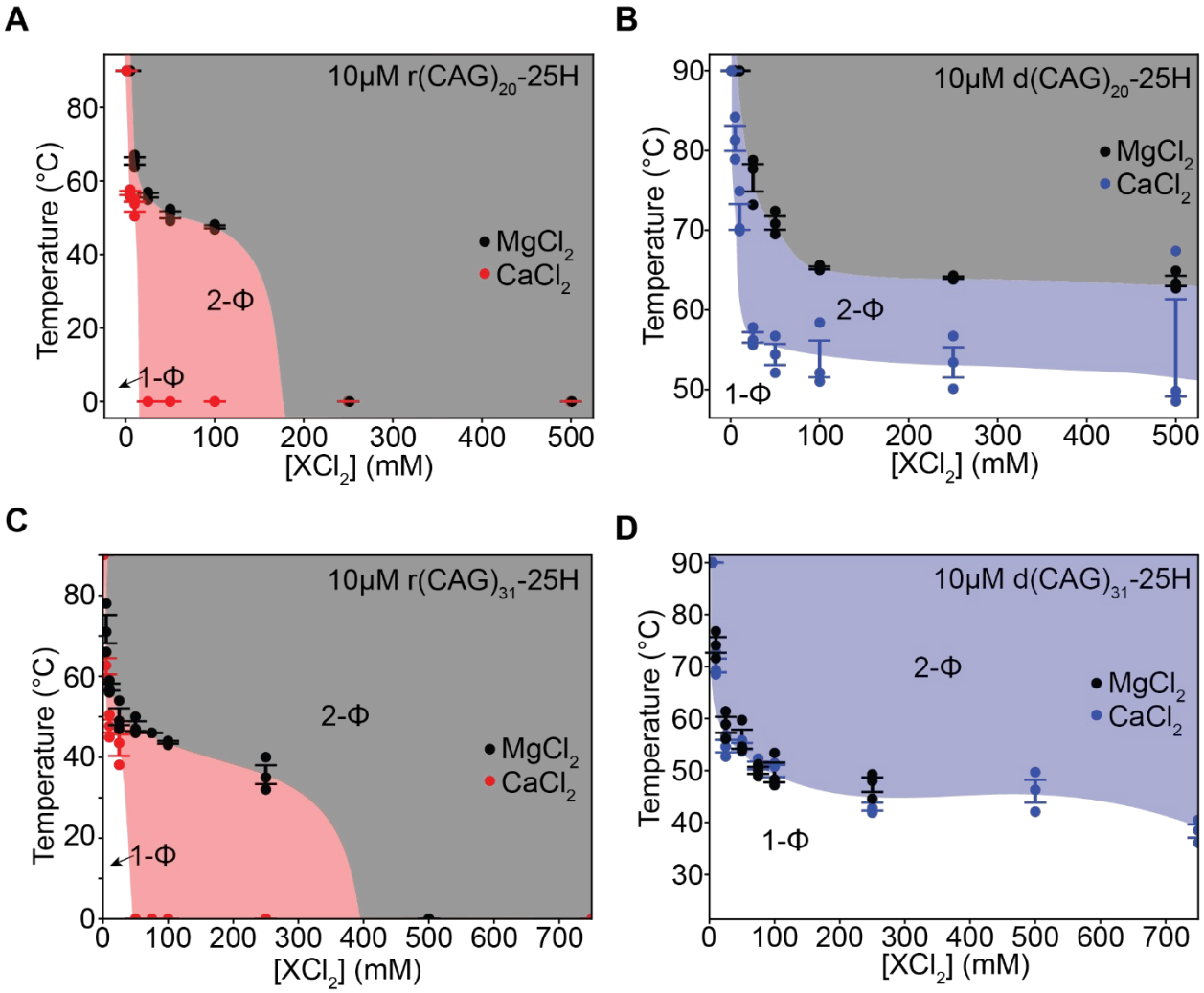

Fig. S23. Comparison of the differential effects of calcium and magnesium on phase separation of $(CAG)_{20}$ and $(CAG)_{31}$ RNA and ssDNA. A. State diagram comparing [$MgCl_2$] (black) to [$CaCl_2$] (red) dependence for $r(CAG)_{20}$. Shading represents the 2-Φ regime for [$MgCl_2$] (grey) to [$CaCl_2$] (red). **B.** State diagram comparing [$MgCl_2$] (black) to [$CaCl_2$] (red) dependence for $d(CAG)_{20}$. Shading represents the 2-Φ regime for [$MgCl_2$] (grey) to [$CaCl_2$] (blue). **C.** State diagram comparing [$MgCl_2$] (black) to [$CaCl_2$] (red) dependence for $r(CAG)_{31}$. Shading represents the 2-Φ regime for [$MgCl_2$] (grey) to [$CaCl_2$] (red). **D.** State diagram comparing [$MgCl_2$] (black) to [$CaCl_2$] (blue) dependence for $d(CAG)_{31}$. Shading represents the 2-Φ regime for [$MgCl_2$] (grey) to [$CaCl_2$] (blue). In all diagrams, red is used to indicate irreversible phase separation while blue is used to indicate reversible phase separation. Buffer notation used: the number in front of "H" indicates the [HEPES] in mM in the buffer.

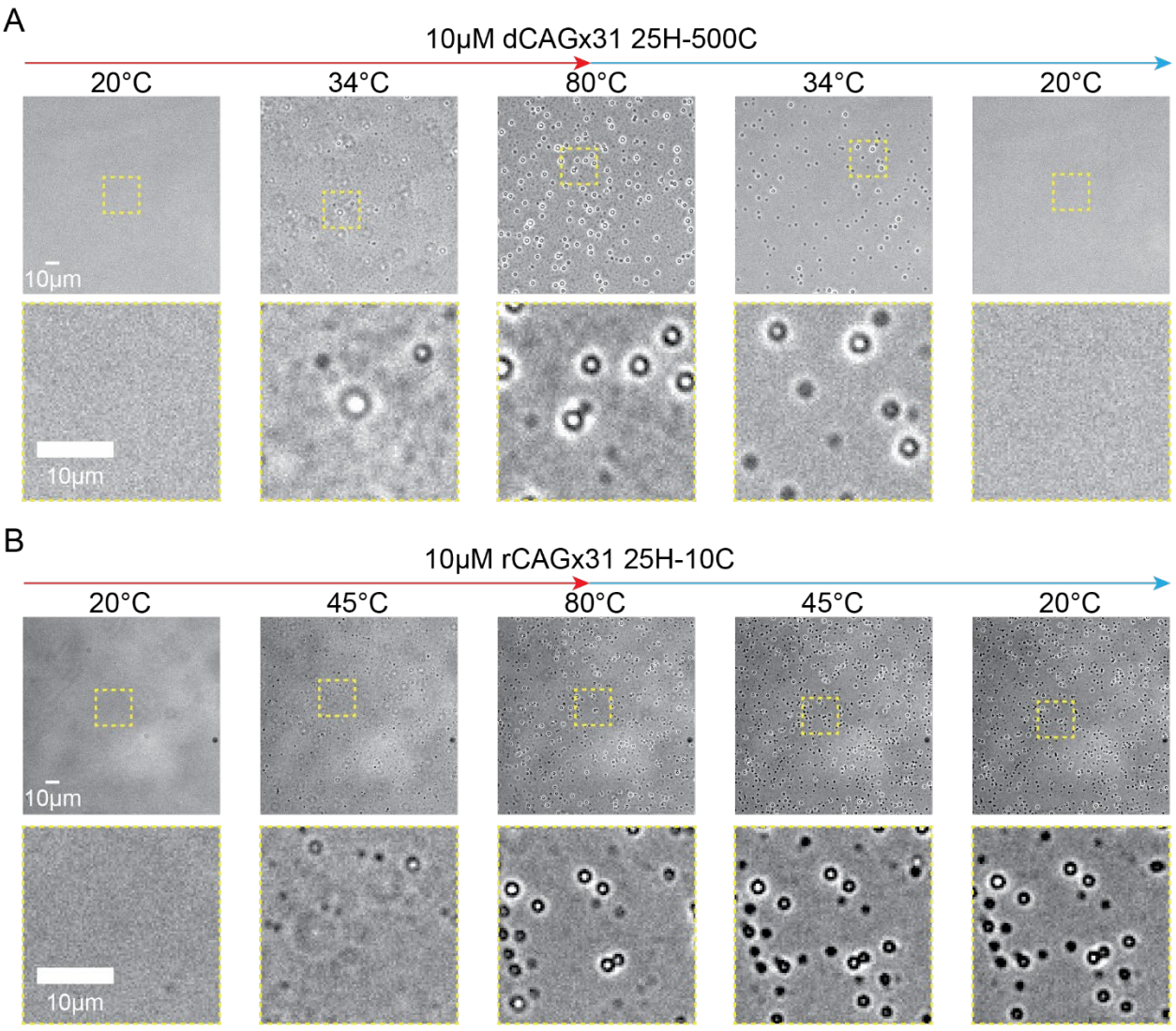

Fig. S24. Brightfield images of the calcium dependent thermoresponsive phase behavior of $d(CAG)_{31}$ compared to $r(CAG)_{31}$. A. Representative images of thermoresponsive phase separation of 10 μM $d(CAG)_{31}$ in a buffer containing 25 mM HEPES, pH 7.5 at RT, and 500 mM $CaCl_2$. The LCPT is 46.3 ± 2.2°C. **B.** Representative images of thermoresponsive phase separation of 10 μM r(CAG)31in a buffer containing 25 mM HEPES, pH 7.5 at RT, and 10 mM $MgCl_2$. The LCPT is 47.7 ± 1.6°C. We note that RNA percolates at relatively lower $[Ca^{+2}]$ while the DNA does not percolate at all conditions tested. The yellow border demarcates the inset shown below each panel. Buffer notation used: the number in front of "H" indicates the [HEPES] in mM and the number in front of "C" indicates the $[CaCl_2]$ in mM in the buffer.

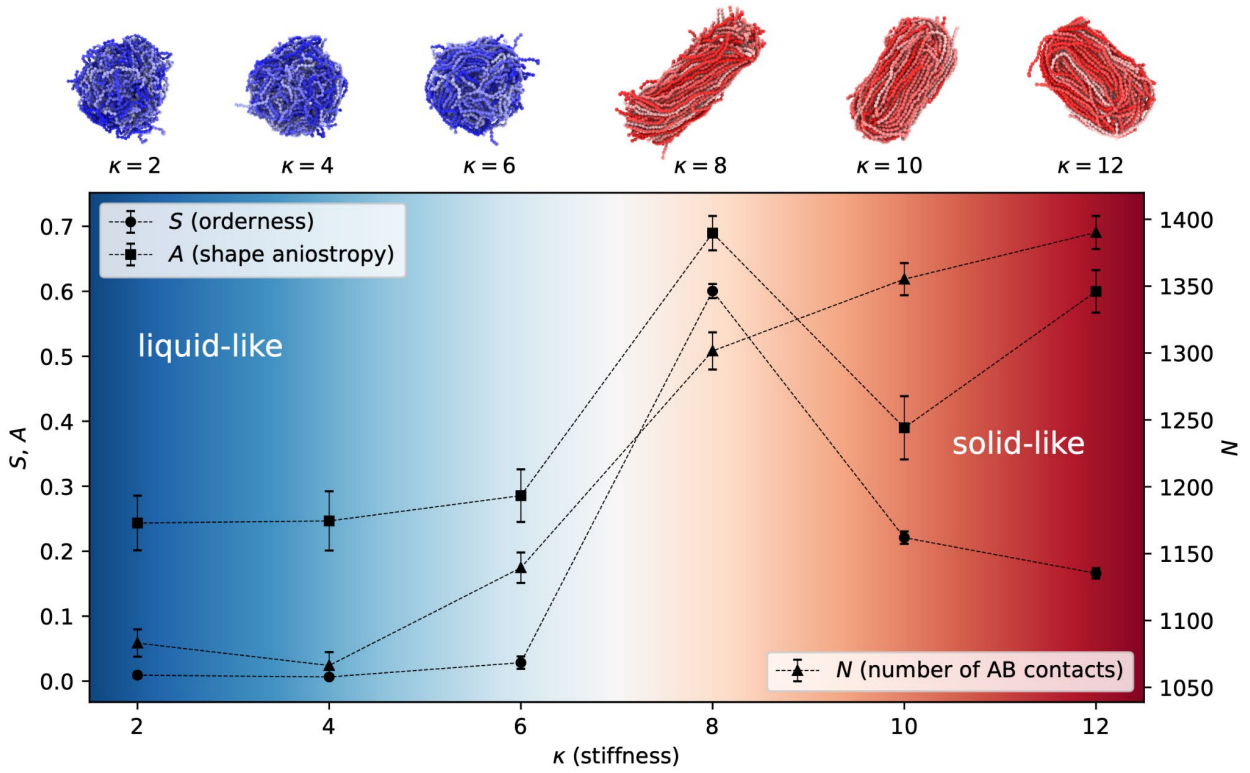

Fig. S25. Effect of bending stiffness on condensate properties. Under the same conditions, minimal model simulations show that increasing the stiffness (κ) can induce a transition from a liquid-like condensate to a dynamically arrested condensate. This transition is characterized by an increase in orderness S, deviation of relative shape anisotropy A, and increase in the number of interchain crosslinks N. The errors are estimated using standard deviation obtained by measuring condensate properties using 1000 snapshots from the last 10,000,000 timesteps, which are sampled every 10,000 steps.

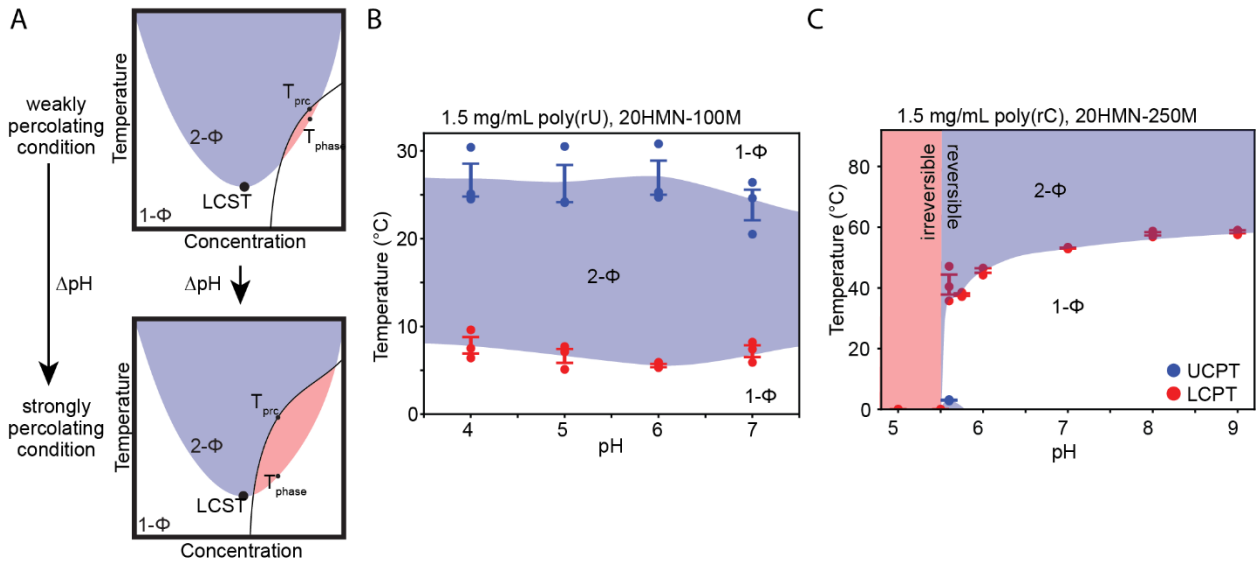

385

386 **Fig. S26. pH dependent percolation and phase separation of RNA. A.** A schematic showing
387 pH-dependent intersection of the percolation line with the binodal line (2-Φ regime). **B.** A state
388 diagram showing the pH dependence of the UCPTs and LCPTs of poly(rU) at 1.5 mg/mL in a
389 buffer containing 20 mM each of HEPES, MES, and NaAc at the specified pH with 100 mM $MgCl_2$.
390 The blue shading indicates the 2-Φ regime which is reversible. **C.** A state diagram showing the
391 pH dependence of the LCPTs of poly(rC) at 1.5 mg/mL in a buffer containing 20mM each of
392 HEPES, MES and NaAc at the specified pH with 100 mM $MgCl_2$. The shading indicates the 2-Φ
393 regime, and the color indicates reversibility (blue) or irreversibility (red). Buffer notation used: the
394 number in front of "HMN" indicates the [HEPES]; [MES]; and [NaAc] in mM, and the number in
395 front of "M" indicates [$MgCl_2$] in mM in each buffer. Error bars represent s.e.m. for n = 3 replicates.

396

397

Name	Sequence	Vendor	Type
$r(CAG)_{31}$	5'-CAGCAGCAGCAGCAGCAGCAGCAGCAGCAGCAGCAGCAGCAGCAGCAGCAGCAGCAGCAGCAG CAGCAGCAGCAGCAGCAGCAGCAG-3'	IDT	RNA
$r(CUG)_{31}$	5'-CUGCUGCUGCUGCUGCUGCUGCUGCUGCUGCUGCUGCUGCUGCUGCUGCUGCUGCUGCUGCUG CUGCUGCUGCUGCUGCUGCUG-3'	IDT	RNA
$r(CGG)_{31}$	5'-CGGCGGCGGCGGCGGCGGCGGCGGCGGCGGCGGCGGCGGCGGCGGCGGCGGCGGCGGCGGCGG CGGCGGCGGCGGCGGCGGCGG-3'	IDT	RNA
$r(CCG)_{31}$	5'-CCGCCGCCGCCGCCGCCGCCGCCGCCGCCGCCGCCGCCGCCGCCGCCGCCGCCGCCGCCGCCG CCGCCGCCGCCGCCGCCGCCG-3'	IDT	RNA
$d(CAG)_{31}$	5'-CAGCAGCAGCAGCAGCAGCAGCAGCAGCAGCAGCAGCAGCAGCAGCAGCAGCAGCAGCAGCAG CAGCAGCAGCAGCAGCAGCAGCAG-3'	IDT	DNA
$d(CTG)_{31}$	5'-CTGCTGCTGCTGCTGCTGCTGCTGCTGCTGCTGCTGCTGCTGCTGCTGCTGCTGCTGCTGCTG CTGCTGCTGCTGCTGCTGCTGCTG-3'	IDT	DNA
$d(CGG)_{31}$	5'-CGGCGGCGGCGGCGGCGGCGGCGGCGGCGGCGGCGGCGGCGGCGGCGGCGGCGGCGGCGGCGG CGGCGGCGGCGGCGGCGGCGG-3'	IDT	DNA
$d(CCG)_{31}$	5'-CCGCCGCCGCCGCCGCCGCCGCCGCCGCCGCCGCCGCCGCCGCCGCCGCCGCCGCCGCCGCCG CCGCCGCCGCCGCCGCCGCCG-3'	IDT	DNA
$r(CAG)_{20}$	5'-CAGCAGCAGCAGCAGCAGCAGCAGCAGCAGCAGCAGCAGCAGCAGCAGCAGCAGCAGCAG3'	IDT	RNA
$d(CAG)_{20}$	5'-CAGCAGCAGCAGCAGCAGCAGCAGCAGCAGCAGCAGCAGCAGCAGCAGCAGCAGCAGCAG3'	IDT	DNA
$r(CmAG)_{20}$	5'-CmAGCmAGCmAGCmAGCmAGCmAGCmAGCmAGCmAGCmAGCmAGCmAGCmAGCmAGCmAG CmAGCmAGCmAGCmAGCmAG3'	Gene Link	RNA
$(TERRA)_{10}$	5'-UUAGGGUUAGGGUUAGGGUUAGGGUUAGGGUUAGGGUUAGGGUUAGGGUUAGGGUUAGGG-3'	IDT	RNA
$(htelo)_{10}$	5'-TTAGGGTTAGGGTTAGGGTTAGGGTTAGGGTTAGGGTTAGGGTTAGGGTTAGGGTTAGGG-3'	IDT	DNA
$d(CAG)_{47}$	5'-CAGCAGCAGCAGCAGCAGCAGCAGCAGCAGCAGCAGCAGCAGCAGCAGCAGCAGCAGCAGCAG CAGCAGCAGCAGCAGCAGCAGCAGCAGCAGCAGCAGCAGCAGCAGCAGCAGCAGCAGCAGCAG CAGCAG-3'	IDT	DNA
$r(CAG)_{47}$	5'-CUGCUGCUGCUGCUGCUGCUGCUGCUGCUGCUGCUGCUGCUGCUGCUGCUGCUGCUGCUGCUG CUGCUGCUGCUGCUGCUGCUGCUGCUGCUGCUGCUGCUGCUGCUGCUGCUGCUGCUGCUGCUG CUGCUG-3'	in vitro transcription	RNA

Table S1. Table of nucleic acid sequences used in experiments.

Movie Captions

Movie S1.

Phase separation of $d(CAG)_{31}$. A sample of 100 μM $d(CAG)_{31}$ in 25 mM Tris-HCl, (pH 7.5 at 25°C) and 50 mM $MgCl_2$ underwent thermal cycling via temperature-controlled microscopy. $d(CAG)_{31}$ phase separated reversibly with a LCPT of 55.3± 0.75°C (n = 3 replicates).

Movie S2.

Phase separation of $r(CAG)_{31}$. A sample of 100 μM $r(CAG)_{31}$ in 25 mM Tris-HCl, (pH 7.5 at 25°C) and 50 mM $MgCl_2$ underwent thermal cycling via temperature-controlled microscopy. $r(CAG)_{31}$ phase separated irreversibly with a LCPT of 40.1 ± 0.96°C (n = 3 replicates).

Movie S3.

Phase separation of $d(CAG)_{20}$. A sample of 100 μM $d(CAG)_{20}$ in 25 mM Tris-HCl, (pH 7.5 at 25°C) and 50 mM $MgCl_2$ underwent thermal cycling via temperature-controlled microscopy. $d(CAG)_{20}$ phase separated reversibly with a LCPT of 72.4 ± 1.71°C (n = 3 replicates).

Movie S4.

Phase separation of $d(CAG)_{47}$. A sample of 100 μM $d(CAG)_{47}$ in 25 mM Tris-HCl, (pH 7.5 at 25°C) and 50 mM $MgCl_2$ underwent thermal cycling via temperature-controlled microscopy. $d(CAG)_{47}$ phase separated reversibly with a LCPT of 46.3 ± 3.0°C (n = 3 replicates).

Movie S5.

Phase separation of $r(CAG)_{31}$. A sample of 100 μM $r(CAG)_{31}$ in 25 mM Tris-HCl, (pH 7.5 at 25°C), 50 mM $MgCl_2$, and 25 mM NaCl underwent thermal cycling via temperature-controlled microscopy. $r(CAG)_{31}$ phase separated irreversibly with a LCPT of 41.3 ± 1.5°C (n = 3 replicates).

Movie S6.

Phase separation of $d(CAG)_{31}$. A sample of 100 μM $d(CAG)_{31}$ in 25 mM Tris-HCl, (pH 7.5 at 25°C), 50 mM $MgCl_2$, and 25 mM NaCl underwent thermal cycling via temperature-controlled microscopy. $d(CAG)_{31}$ phase separated reversibly with a LCPT of 50.1± 2.5°C (n = 3 replicates).

Movie S7.

Phase separation of $r(CUG)_{31}$. A sample of 100 μM $r(CUG)_{31}$ in 25 mM Tris-HCl, (pH 7.5 at 25°C), 50 mM $MgCl_2$, and 25 mM NaCl underwent thermal cycling via temperature-controlled microscopy. $r(CUG)_{31}$ phase separated reversibly with a LCPT of 59.2 ± 2.4°C (n = 3 replicates).

Movie S8.

Phase separation of $d(CTG)_{31}$. A sample of 100 μM $d(CTG)_{31}$ in 25 mM Tris-HCl, (pH 7.5 at 25°C), 50 mM $MgCl_2$, and 25 mM NaCl underwent thermal cycling via temperature-controlled microscopy. $d(CTG)_{31}$ phase separated reversibly with a LCPT of 72.9 ± 2.0°C (n = 3 replicates).

Movie S9.

Phase separation of $r(CGG)_{31}$. A sample of 100 μM $r(CGG)_{31}$ in 25 mM Tris-HCl, (pH 7.5 at 25°C), 50 mM $MgCl_2$, and 25 mM NaCl underwent thermal cycling via temperature-controlled microscopy. $r(CGG)_{31}$ phase separated irreversibly with a LCPT of 50.5 ± 0.73°C (n = 3 replicates).

Movie S10.

Phase separation of $d(CGG)_{31}$. A sample of 100 μM $d(CGG)_{31}$ in 25 mM Tris-HCl, (pH 7.5 at 25°C), 50 mM $MgCl_2$, and 25 mM NaCl underwent thermal cycling via temperature-controlled microscopy. $d(CGG)_{31}$ phase separated irreversibly with a LCPT of 60.1 ± 0.87°C (n = 3 replicates).

Movie S11.

Phase separation of $r(CCG)_{31}$. A sample of 100 μM $r(CCG)_{31}$ in 25 mM Tris-HCl, (pH 7.5 at 25°C), 50 mM $MgCl_2$, and 25 mM NaCl underwent thermal cycling via temperature-controlled microscopy. $r(CCG)_{31}$ phase separated reversibly with a LCPT of 51.8 ± 0.74°C (n = 3 replicates).

Movie S12.

Phase separation of $d(CCG)_{31}$. A sample of 100 μM $d(CCG)_{31}$ in 25 mM Tris-HCl, (pH 7.5 at 25°C), 50 mM $MgCl_2$, and 25 mM NaCl underwent thermal cycling via temperature-controlled microscopy. $d(CCG)_{31}$ phase separated reversibly with a LCPT of 52.4 ± 0.96°C (n = 3 replicates).

Movie S13.

Phase separation of $(TERRA)_{10}$. A sample of 50 μM $(TERRA)_{10}$ in 25 mM Tris-HCl, (pH 7.5 at 25°C) and 6.25 mM $MgCl_2$ underwent thermal cycling via temperature-controlled microscopy. $(TERRA)_{10}$ phase separated irreversibly with a LCPT of 65.0 ± 1.8°C (n = 3 replicates). This video is remade from Mahendran et al., 2024 [19].

Movie S14.

Reversible phase separation of $(htelo)_{10}$. A sample of 50 μM $(htelo)_{10}$ in 25 mM Tris-HCl, (pH 7.5 at 25°C) and 50 mM $MgCl_2$ underwent thermal cycling via temperature-controlled microscopy. $d(telo)_{10}$ phase separated reversibly with a LCPT of 60.4 ± 0.48°C (n = 3 replicates).

Movie S15.

Irreversible phase separation of $(htelo)_{10}$. A sample of 50 μM $(htelo)_{10}$ in 25 mM Tris-HCl, (pH 7.5 at 25°C) and 100 mM $MgCl_2$ underwent thermal cycling via temperature-controlled microscopy. $d(telo)_{10}$ phase separated irreversibly with a LCPT of 53.7 ± 0.78°C (n = 3 replicates).

Movie S16.

Percolation of $(TERRA)_{10}$. A sample of 50 μM $(TERRA)_{10}$ in 25 mM Tris-HCl, (pH 7.5 at 25°C) and 50 mM $MgCl_2$ underwent thermal cycling via temperature-controlled microscopy. $(TERRA)_{10}$ clusters underwent shape relaxation upon heating from irregular clusters to spherical condensates (n = 3 replicates).

Movie S17.

Phase separation of $r(CmAG)_{20}$. A sample of 10 μM $r(CmAG)_{20}$ in 50 mM HEPES, (pH 7.5 at 25°C) and 50 mM $MgCl_2$ underwent thermal cycling via temperature-controlled microscopy. $r(CmAG)_{20}$ phase separated reversibly with a LCPT of 57.7 ± 0.81°C (n = 3 replicates).

Movie S18.

Phase separation of $r(CAG)_{20}$. A sample of 10 μM $r(CAG)_{20}$ in 50 mM HEPES, (pH 7.5 at 25°C) and 50 mM $MgCl_2$ underwent thermal cycling via temperature-controlled microscopy. $r(CAG)_{20}$ phase separated irreversibly with a LCPT of 51.4 ± 2.49°C (n = 3 replicates).

Movie S19.

Ca^{+2} ion dependent phase separation of $r(CAG)_{31}$. A sample of 10 μM $r(CAG)_{31}$ in 25 mM HEPES, (pH 7.5 at 25°C) and 10 mM $CaCl_2$ underwent thermal cycling via temperature-controlled microscopy. $r(CAG)_{31}$ phase separated irreversibly with a LCPT of 44.9 ± 1.6°C (n = 3 replicates).

Movie S20.

Reversible condensation of poly(rC). A sample of 1.5 mg/mL poly(rC) in 20 mM HEPES-MES-NaAc (pH 5.75 at 25°C) and 250 mM $MgCl_2$ underwent thermal cycling via temperature-controlled microscopy. Poly(rC) phase separated reversibly with a LCPT of 38.5 ± 0.4°C (n = 3 replicates).

Movie S21.

Irreversible condensation of poly(rC). A sample of 1.5 mg/mL poly(rC) in 20 mM HEPES-MES-NaAc (pH 5.6 at 25°C) and 250 mM $MgCl_2$ underwent thermal cycling via temperature-controlled microscopy. Poly(rC) phase separated irreversibly with a LCPT of 35.7 ± 3.3°C (n = 3 replicates).

Movie S22.

Percolation of poly(rC) condensates. A sample of 1.5 mg/mL poly(rC) in 20 mM HEPES-MES-NaAc, (pH 5.5 at 25°C) and 250 mM $MgCl_2$ underwent thermal cycling via temperature-controlled microscopy. Poly(rC) clusters underwent shape relaxation upon heating (n = 3 replicates).

Movie S23.

Phase separation of poly(rU). A sample of 1.5 mg/mL poly(rU) in 25 mM Tris-HCl, (pH 7.5 at 25°C) and 400 mM $MgCl_2$ underwent thermal cycling via temperature-controlled microscopy. Poly(rU) phase separated reversibly with a UCPT of 24.2 ± 0.5°C and a LCPT of 1.1 ± 0.3°C (n = 3 replicates). This video is reproduced from Wadsworth et al., 2023 [17].

References

1 Denning, E. J., Priyakumar, U. D., Nilsson, L. & Mackerell Jr, A. D. Impact of 2′-hydroxyl sampling on the conformational properties of RNA: update of the CHARMM all-atom additive force field for RNA. *Journal of computational chemistry* **32**, 1929-1943 (2011).

2 Hart, K. *et al.* Optimization of the CHARMM additive force field for DNA: Improved treatment of the BI/BII conformational equilibrium. *Journal of chemical theory and computation* **8**, 348-362 (2012).

3 MacKerell Jr, A. D. *et al.* All-atom empirical potential for molecular modeling and dynamics studies of proteins. *The journal of physical chemistry B* **102**, 3586-3616 (1998).

4 Xu, Y., Vanommeslaeghe, K., Aleksandrov, A., MacKerell Jr, A. D. & Nilsson, L. Additive CHARMM force field for naturally occurring modified ribonucleotides. *Journal of computational chemistry* **37**, 896-912 (2016).

5 Abraham, M. *et al.* GROMACS 2023.1 Manual. *GROMACS: Groningen, The Netherlands* (2023).

6 Abraham, M. J. *et al.* GROMACS: High performance molecular simulations through multi-level parallelism from laptops to supercomputers. *SoftwareX* **1**, 19-25 (2015).

7 Jo, S., Kim, T., Iyer, V. G. & Im, W. CHARMM-GUI: a web-based graphical user interface for CHARMM. *Journal of computational chemistry* **29**, 1859-1865 (2008).

8 Lee, J. *et al.* CHARMM-GUI input generator for NAMD, GROMACS, AMBER, OpenMM, and CHARMM/OpenMM simulations using the CHARMM36 additive force field. *Biophysical journal* **110**, 641a (2016).

9 Darden, T., York, D. & Pedersen, L. Particle mesh Ewald: An N· log (N) method for Ewald sums in large systems. *The Journal of chemical physics* **98**, 10089-10092 (1993).

10 Hess, B., Bekker, H., Berendsen, H. J. & Fraaije, J. G. LINCS: a linear constraint solver for molecular simulations. *Journal of computational chemistry* **18**, 1463-1472 (1997).

11 Michaud-Agrawal, N., Denning, E. J., Woolf, T. B. & Beckstein, O. MDAnalysis: a toolkit for the analysis of molecular dynamics simulations. *Journal of computational chemistry* **32**, 2319-2327 (2011).

12 DeLano, W. L. Pymol: An open-source molecular graphics tool. *CCP4 Newsl. Protein Crystallogr* **40**, 82-92 (2002).

13 Meng, E. C. *et al.* UCSF ChimeraX: Tools for structure building and analysis. *Protein Science* **32**, e4792 (2023).

14 Thompson, A. P. *et al.* LAMMPS-a flexible simulation tool for particle-based materials modeling at the atomic, meso, and continuum scales. *Computer Physics Communications* **271**, 108171 (2022).

15 Stukowski, A. Modeling Simul Mater. *Sci. Eng* **18**, 015012 (2010).

16 Mahendran, T. S., Wadsworth, G. M., Singh, A. & Banerjee, P. R. Biomolecular Condensates Can Enhance Pathological RNA Clustering. *bioRxiv*, 2024.2006. 2011.598371 (2024).

17 Wadsworth, G. M. *et al.* RNAs undergo phase transitions with lower critical solution temperatures. *Nature Chemistry*, 1-12 (2023).

18 Brooke, D., Movahed, N. & Bothner, B. Universal buffers for use in biochemistry and biophysical experiments. *AIMS biophysics* **2**, 336 (2015).

19 Mahendran, T. S., Wadsworth, G. M., Singh, A. & Banerjee, P. R. Biomolecular Condensates Can Enhance Pathological RNA Clustering. *bioRxiv* (2024).